The thermal infrared optical depth of mineral dust retrieved from integrated CALIOP and IIR observations

Jianyu Zheng[1], Zhibo Zhang[1], Anne Garnier[2], Hongbin Yu[3], Qianqian Song[1], Chenxi Wang[1], Philippe Dubuisson[4], and Claudia Di Biagio[5]

[1]University of Maryland Baltimore County
[2]Science Systems and Applications, Inc.
[3]NASA Goddard Space Flight Center
[4]Université de Lille
[5]Université de Paris and Univ Paris Est Creteil, CNRS, LISA

November 21, 2022

Abstract

Recent studies reveal that a higher fraction of coarse mineral dust particles than that estimated by climate model simulations has been observed in the atmosphere, leading to a more significant positive (i.e., warming) longwave (LW) thermal infrared (TIR) direct radiative effect (DRE). However, the magnitude of this DRE remains highly uncertain because our understanding of the radiative properties, quantitatively represented by the optical depth of dust, especially information on the TIR, remains limited. This study presents a simple approach to retrieve the thermal infrared dust aerosol optical depth (DAODTIR) over oceans during nighttime using the observations from the Infrared Imaging Radiometer (IIR) and the Cloud-Aerosol Lidar with Orthogonal Polarization (CALIOP) onboard CALIPSO. For each cloud-free dust-laden profile identified by the IIR-CALIOP observation, a Lookup-Table (LUT) of the 10.6 μm IIR band brightness temperatures difference (dBT) under different DAODTIR with respect to their dust-free BTs is constructed based on the CALIOP retrieved dust vertical profile and pre-assumed dust scattering properties using a fast radiative transfer model. Then the DAODTIR is retrieved by projecting the IIR-observed dBT on the LUT. Sensitivity studies show that the DAODTIR retrieval at 10.6 μm is more susceptible to the dust particle size distribution (PSD) assumption than dust refractive indices. To estimate the uncertainty caused by PSD assumption, two DAODTIR retrieval products, one based on the dust PSD from the AERONET at Cape Verde and the other on an in situ measured PSD from the recent Fennec campaign, are provided. The retrieval uncertainty is mainly contributed by the BT difference between the observation and simulation using auxiliary atmospheric data. The climatology of the retrieval from 2013 to 2019 shows confident spatiotemporal variations of DAODTIR with the global-averaged value of 0.006 and 0.008 based on different pre-assumed dust PSDs. Climatological results agree reasonably well with two independent DAODTIR retrieval products based on the Infrared Atmospheric Sounding Interferometer (IASI) over the active dust transport regions, such as North and Tropical Atlantic (r = 0.904 and 0.819) and Indian Ocean (r = 0.832). The seasonal and interannual variation is also well-compared (r = 0.758) with AERONET coarse-mode AOD at 97 selected sites. The synergic CALIOP observation allows the retrieved DAODTIR to directly compare with the extrapolated DAODTIR from DAOD in visible (i.e., 532 nm), which helps evaluate the observational constraints on DAODTIR. This study offers a unique prospect of collocating active lidar and passive IR observations for retrieving dust DAODTIR.

The thermal infrared optical depth of mineral dust retrieved from integrated CALIOP and IIR observations

Jianyu Zheng[1,2], Zhibo Zhang[1,2,*], Anne Garnier[3,4], Hongbin Yu[5], Qianqian Song[1,2], Chenxi Wang[2,5], Philippe Dubuisson[6], Claudia Di Biagio[7]

[1]Department of Physics, University of Maryland at Baltimore County, Baltimore, Maryland, USA

[2]Joint Center for Earth Systems Technology, University of Maryland Baltimore County, Baltimore, Maryland, USA

[3]Science Systems and Applications, Inc., Hampton, Virginia, USA

[4]NASA Langley Research Center, Hampton, Virginia

[5]NASA Goddard Space Flight Center, Greenbelt, Maryland, USA

[6]Laboratoire d'Optique Atmosphérique, Université de Lille, Lille, France

[7]Université de Paris and Univ Paris Est Creteil, CNRS, LISA, F-75013 Paris, France

**Correspondence to: Zhibo Zhang (zzbatmos@umbc.edu)*

Abstract

Recent studies reveal that a higher fraction of coarse mineral dust particles than that estimated by climate model simulations has been observed in the atmosphere, leading to a more significant positive (i.e., warming) longwave (LW) thermal infrared (TIR) direct radiative effect (DRE). However, the magnitude of this DRE remains highly uncertain because our understanding of the radiative properties, quantitatively represented by the optical depth of dust, especially information on the TIR, remains limited. This study presents a simple approach to retrieve the thermal infrared dust aerosol optical depth ($DAOD_{TIR}$) over oceans during nighttime using the observations from the Infrared Imaging Radiometer (IIR) and the Cloud-Aerosol Lidar with Orthogonal Polarization (CALIOP) onboard CALIPSO. For each cloud-free dust-laden profile identified by the IIR-CALIOP observation, a Lookup-Table (LUT) of the 10.6 μm IIR band brightness temperatures difference (dBT) under different $DAOD_{TIR}$ with respect to their dust-free BTs is constructed based on the CALIOP retrieved dust vertical profile and pre-assumed dust scattering properties using a fast radiative transfer model. Then the $DAOD_{TIR}$ is retrieved by projecting the IIR-observed dBT on the LUT. Sensitivity studies show that the $DAOD_{TIR}$ retrieval at 10.6 μm is more susceptible to the dust particle size distribution (PSD) assumption than dust refractive indices. To estimate the uncertainty caused by PSD assumption, two $DAOD_{TIR}$ retrieval products, one based on the dust PSD from the AERONET at Cape Verde and the other on an in situ measured PSD from the recent Fennec campaign, are provided. The retrieval uncertainty is mainly contributed by the BT difference between the observation and simulation using auxiliary atmospheric data. The climatology of the retrieval from 2013 to 2019 shows confident spatiotemporal variations of $DAOD_{TIR}$ with the global-averaged value of 0.006 and 0.008 based on different pre-assumed dust PSDs. Climatological results agree reasonably well with two independent $DAOD_{TIR}$ retrieval

products based on the Infrared Atmospheric Sounding Interferometer (IASI) over the active dust transport regions, such as North and Tropical Atlantic (r = 0.904 and 0.819) and Indian Ocean (r = 0.832). The seasonal and interannual variation is also well-compared (r = 0.758) with AERONET coarse-mode AOD at 97 selected sites. The synergic CALIOP observation allows the retrieved $DAOD_{TIR}$ to directly compare with the extrapolated $DAOD_{TIR}$ from DAOD in visible (i.e., 532 nm), which helps evaluate the observational constraints on $DAOD_{TIR}$. This study offers a unique prospect of collocating active lidar and passive IR observations for retrieving dust $DAOD_{TIR}$.

Keywords: Aerosol, Dust, Thermal infrared, IIR, CALIOP

1. Introduction

Mineral dust (hereafter referred to as dust for short) is a major component of atmospheric aerosols, originating mainly from arid and semi-arid deserts, dry lake beds, and areas with extreme soil moisture deficits and reduced vegetation cover (Choobari et al. 2014). Once aloft, dust aerosols may be carried by winds for long-range transport of an intercontinental scale, such as the trans-Atlantic transport of North African dust (Chiapello and Moulin 2002; Di Biagio et al. 2021), transport of dust plumes from the Arabian Peninsula over the Arabian Sea and the Indian Ocean in summer, and trans-pacific transport of Asia dust in spring (Goudie and Middleton 2006). Meanwhile, they can influence the Earth-Atmosphere system's radiative energy budget and thermodynamic structure through aerosol-radiation interactions (ARI). Over dark ocean, the scattering effect of dust dominates its interactions with shortwave solar radiation (referred to as "SW"), leading to a negative (i.e., cooling) SW direct radiative effect (DRE_{SW}) at the top of atmosphere (TOA). Different from most other aerosol types that are small in size (below 1 μm), dust, whose particle size distribution (PSD) is in surface, volume and mass usually dominated by the coarse mode (diameter > 1 μm), also has significant radiative effects in the longwave (referred to as “LW”), where the absorption effect is dominant, resulting in a positive (i.e., warming) LW DRE (DRE_{LW}) (Torres et al. 1998; Yu et al. 2006). The net radiative effect of dust, as the sum of DRE_{SW} and DRE_{LW}, has significant impacts on the planetary energy balance (Tegen et al. 1996; Yu et al. 2006; Song et al. 2018), as well as regional weather and climate variability (Tegen and Lacis 1996; Evan et al. 2006). Despite this qualitative understanding, quantitative estimates of dust DRE remain highly uncertain. Several recent studies argued that most global climate models (GCMs) tend to underestimate the fraction of coarse dust particle as a larger amount of them have been observed (Adebiyi and Kok 2020; Kok et al. 2017; Ryder et al. 2013b). As a result, GCMs,

in turn, overestimate dust DRE_{SW} and underestimate DRE_{LW} (Kok et al.,2017; Di Biagio et al. 2020). In addition to the DRE, dust can also alter various micro- and macro-physical properties of clouds and their evolution and lifetime through aerosol-cloud interactions (ACI). Moreover, dust storms and plumes can degrade air quality and generate adverse impacts on human health (Griffin, 2007; Querol et al., 2019).

To better quantify the aforementioned influences of dust on radiation, cloud and air quality, we need continuous observations of dust spatial and vertical distribution and key optical and microphysical properties, broadly represented by the aerosol optical depth (AOD) of dust (DAOD). Presently, satellite-based remote sensing is the only way to obtain such observations on a global scale. Over the last few decades, numerous techniques have been developed to retrieve aerosol properties, in particular the AOD, from satellite observations, such as the Moderate Resolution Imaging Spectroradiometer (MODIS), the multi-angle imaging spectroradiometer (MISR), the Visible Infrared Imaging Radiometer Suite (VIIRS), the Cloud-Aerosol Lidar with Orthogonal Polarization (CALIOP) and the Cloud-Aerosol Transport System (CATS), etc. Most of these techniques operate in the visible (referred to as "VIS") to near-infrared spectral region because most aerosols, such as smoke and sulfate, only have significant radiative effects in the VIS (Satheesh and Moorthy 2005). However, as mentioned above, with a large amount of coarse particles, dust also interacts with radiation in the thermal infrared (referred to as “TIR” for brevity) spectral region, allowing the retrieval of DAOD based on TIR observations (Sokolik et al. 1998).

Satellite-based retrievals of the DAOD in TIR (i.e., $DAOD_{TIR}$), are essential and highly useful for many purposes. First, the VIS retrieval requires solar illumination and is therefore only available during the daytime. In contrast, the TIR retrieval does not have such limitations, available at both daytime and nighttime. Second, as shown in Capelle et al. (2014), merely extrapolating the

retrieved AOD in VIS to TIR without any observational constraint can lead to substantial error and uncertainty. Therefore, with a better satellite-based dust TIR retrieval, the dust extinction spectrum from VIS to TIR can be improved by connecting the retrieval from both spectra (Klüser et al. 2012). Third, the DRE_{LW} of dust is more sensitive to the coarse mode of the dust and, therefore, more directly connected to the $DAOD_{TIR}$ rather than the $DAOD_{VIS}$ (Capelle et al. 2014; Peyridieu et al. 2010). For example, Song et al. (2018) showed that two dust models, one with a larger size and less absorptive VIS refractive index, and the other with a smaller size and more absorptive VIS refractive index, can have almost identical DRE_{SW} provided the same retrieved $DAOD_{VIS}$. However, the two have pretty different DRE_{LW} because of the difference in $DAOD_{TIR}$ extrapolated based on the assumed dust models, attesting to the need for observation-based retrievals of $DAOD_{TIR}$.

Although satellite based TIR observations are abundant, quantitative retrievals of the TIR dust optical properties are still limited compared to the VIS products due to two major challenges. First, the radiative signal of dust in the TIR is generally weaker due to the relatively small $DAOD_{TIR}$ compared with, for example, clouds. As a result, the noise from atmospheric absorptions in TIR can lead to significant $DAOD_{TIR}$ retrieval uncertainties. The second challenge is that a reliable TIR-based retrieval of DAOD requires precise a knowledge of the dust layer's vertical location and corresponding temperature profile. For these reasons, most of the current $DAOD_{TIR}$ retrievals are based on observations from hyperspectral sounders, such as the Infrared Atmospheric Sounding Interferometer (IASI) and the Atmospheric Infra-Red Sounder (AIRS) (Klüser et al. 2012; Peyridieu et al. 2010; Pierangelo et al. 2004). The high spectral resolution of these instruments allows a careful channel selection in atmospheric window bands to achieve a better signal-to-noise ratio for the retrieval. The observed spectra also provide enough information

content to retrieve both $DAOD_{TIR}$ and dust layer's vertical location. For instance, Pierangelo et al. (2004) demonstrated that DAOD at 10 μm and dust mean altitude could be retrieved by matching the BT difference between the computed and the observed BT in 8 selected channels. Later, Klüser et al. (2011) modified this method to utilize observed dust TIR spectra from IASI operating since 2007 by using the Singular Vector Decomposition (SVD) method to retrieve both $DAOD_{TIR}$ and dust altitude. The 10+ years of IASI-based near-global retrievals of $DAOD_{TIR}$ have proved to be an instrumental dataset for studying dust transport and radiative effects and evaluating dust simulations in climate models (Capelle et al. 2018). Beyond the $DAOD_{TIR}$, Cuesta et al. (2015) developed a new method to retrieve dust vertical profile for major dust outbreaks. Despite these successes, hyperspectral-based dust retrievals also face several challenges and limitations. First, hyperspectral sounders usually have a coarser spatial resolution (e.g., IASI ~ 12 km) than TIR imagers (e.g., IIR ~ 1 km resolution). At this scale, a large fraction of their observations could be contaminated by sub-pixel clouds and thereby overestimated the dust extinction signal (Kaplan 2013; Martins et al. 2002; Xia et al. 2004). Secondly, the retrieval of dust altitude is usually less accurate than what can be achieved by active sensors such as CALIOP and CATS. The inaccurate dust vertical height would, in turn, affect the accuracy of $DAOD_{TIR}$ retrieval. Moreover, the development of a hyperspectral retrieval algorithm that usually involves numerous bands can be rather challenging.

This paper explores an alternative method to retrieve nighttime $DAOD_{TIR}$ over oceans (as explained in section 2.2) based on the integrated observations from CALIOP and the Infrared Imaging Radiometer (IIR) onboard the CALIPSO mission. As an active lidar, CALIOP provides accurate information on the vertical location of dust and cloud masking. The IIR provides observations in three TIR bands, from which the $DAOD_{TIR}$ can be retrieved. In comparison with

the hyperspectral-based methods, our algorithm is unique and has several advantages. First of all, the high sensitivity of CALIOP to clouds and the small spatial resolution of IIR (i.e., 1 km) enables a better cloud masking to avoid potential contamination by sub-pixel clouds. Second, as explained later, the unique depolarization observation of CALIOP provides a way to detect a dust layer and specify its vertical profile. With this advantage, the $DAOD_{TIR}$ can be retrieved from a single IIR band using a relatively simple algorithm, although a few a priori assumptions of dust properties, such as dust particle size, shape and complex refractive index, are needed. In the rest of this paper, we introduce the integrated IIR/CALIOP observation and the radiative transfer model in section 2. The implementation of the $DAOD_{TIR}$ retrieval algorithm is explained in section 3. Section 4 shows the spatiotemporal patterns of the retrieval results and the comparison with IASI retrievals and ground-based AERONET measurement, followed by the summaries and conclusions for the remarks in section 5.

2. Data and model

2.1 CALIOP and IIR observations

The CALIOP level-2 retrieval algorithm detects aerosol layers and records their top and bottom heights and layer integrated properties using a "feature finder" algorithm and cloud-aerosol discrimination (CAD) algorithm (Kim et al. 2018; Liu et al. 2019; Liu et al. 2009). The extinction of an identified aerosol layer is then derived from the attenuated backscatter profile using a priori extinction-to-backscatter ratios (i.e., lidar ratios) based on aerosol sub-types (Young et al. 2018; Young et al. 2013). The aerosol sub-type is determined based on the estimated particulate depolarization ratio (DPR), the color ratio, the layer attenuated backscatter, and the detected aerosol layers height (Kim et al. 2018). Note that the CALIOP operational aerosol product does not provide the specific dust extinction profile when dust is mixed with other types of aerosols (e.g., polluted dust and dusty marine). To alleviate this issue, instead of using the aerosol sub-type information, we mainly use the DPR along with the CAD score from the level-2 aerosol profile product ("CAL_LID_L2_05kmAPro") to estimate the portion of the attenuated backscatter profiles contributed by dust aerosols, and then to obtain the dust aerosol extinction profiles and column DAOD (see section 3.1 for detail). The derived dust aerosol extinction profiles further serve as the dust aerosol vertical distribution for the $DAOD_{TIR}$ retrieval.

The IIR provides measurements of the upwelling radiances in three TIR channels centered around 8.65, 10.6, and 12.05 μm with a medium spectral resolution of 0.9, 0.6, and 1.0 μm, respectively. The instantaneous field of view of IIR is 64 km x 64 km with a pixel size of 1 km by 1 km centered on the CALIOP ground track. The instrument is regularly calibrated using images from cold (about 4 K) deep-space views and a warm blackbody source of 25 °C. The calibrated radiances reported in the IIR Level 1b product are further represented by equivalent brightness

temperatures (BTs) computed using Planck's law and the relevant instrument spectral response functions (SRF) (see Figure 5 (black dash lines)) in the Level 2 product. Recent updates of the calibration corrected the residual systematic bias in the northern hemisphere. A detailed introduction of the IIR instrument and its calibration process is shown in Garnier et al. (2018). The noise equivalent differential temperature and calibration accuracy was assessed by the Centre National d'Etudes Spatiales (CNES) (Garnier et al. 2012). The instrument exhibits an intrinsic 1-sigma noise equivalent to 0.2~0.3 K for a scene temperature of 210 K that improves to 0.1~0.15 K at 250 K and above (see Table 1 in Garnier et al., 2012). In this study, the cloud-free dust-laden cases are rarely lower than 250K. Taking the calibration short term instability (0.1 K) into account, we estimated random measurement uncertainties for each 1-km IIR pixel with ± 0.15 K, ± 0.2 K and ± 0.17 K in the three IIR channels, respectively.

Table 1 lists all variables with the specific values from the Version 4 Level-2 CALIOP aerosol profile product and the Version 4 Level-2 IIR along-track product ("CAL_IIR_L2_Track") used in this study. Beyond the BT measurements, the CAL_IIR_L2_Track product also provides a background reference flag (defined as "Was_Cleared_Flag_1km") to report the number of clouds seen by the 1-km IIR pixel that CALIOP also detected at single-shot resolution (i.e., 333 m) but that were cleared from the CALIOP 5-km layer products to improve the detection of aerosols at coarser spatial resolutions (Vaughan et al. 2005). It helps identify confident cloud-free aerosol profiles for the derivation of the vertical distribution of dust extinction. The level-2 CALIOP aerosol products have a 5-km along-track spatial resolution, while the level-2 IIR products are in 1-km resolution. To match these two datasets, we match the 5-km CALIOP segments to five successive 1-km IIR footprints.

Table 1 Variables of level-2 CALIOP and IIR products that are used in this study

Products	Variable	Value is used
CAL_IIR_L2_Track	Type_of_scene	Cloud-free clean sky (10)
	Was_Cleared_Flag_1km	No single-shot cloud (0)
	TGeotype	Open Water (1700)
	Brightness_Temperature	All
		Ocean only
	Surface_Emissivity	(0.971, 0.984, 0.982
		at 8.65, 10.6, 12.05 μm)
	IIR_Data_Quality_Flag	Calibrated radiances (0)
CAL_LID_L2_05kmAPro	CAD_score	-100 < CAD < -90
	Particulate_Depolarization_Ratio_Profile_532	All
	Particulate_Depolarization_Ratio_Uncertainty_532	< 0.18
	Extinction_QC_Flag_532	0,1,16,18
	Total_Backscatter_Coefficient_532	All
	Atmospheric_Volume_Description	Feature types for cloud detection

200

2.2 The radiative transfer models and reanalysis data

The backbone of our $DAOD_{TIR}$ retrieval algorithm is the FASt radiative transfer code with the Discrete Ordinate Method (FASDOM) developed by Dubuisson et al. (2005). This radiative transfer model (RTM) uses the correlated *k*-distribution method tailored to the IIR SRFs to
205 calculate the atmospheric gas absorptions. With a full account for multiple scattering, the radiative transfer equation is solved by the coupled discrete ordinate radiative transfer code (DISORT) developed by Stamnes et al. (1988). The FASDOM code inputs include atmospheric profiles (temperature, water vapor and ozone), surface temperature, surface emissivity, aerosol layer location in atmospheric profiles, aerosol layer optical depth (OD) and spectral radiative properties

(i.e., single-scattering albedo and asymmetry factor). The FASDOM code has been thoroughly evaluated by comparing the combined line-by-line and DISORT radiative transfer code. Simulations have shown that the accuracy is generally better than 0.3K (Dubuisson et al. 2005; Dubuisson et al. 2008).

Implementing the radiative transfer simulation for global satellite observations requires a reliable dataset of atmospheric states with relatively high spatial and temporal resolution. In this study, we use the instantaneous assimilated atmospheric profiles and surface temperature from Version 2 Modern-Era Retrospective analysis for Research and Applications (MERRA-2) as RTMs' input. The atmospheric profiles from MERRA-2 "inst3_3d_asm_Nv" product have a gridded horizontal resolution of 0.5° latitude × 0.625° longitude and 72 pressure levels from the surface to 0.01 hPa with a 3-hour time step. The surface temperature from "inst1_2d_asm_Nx" product shares the exact horizontal resolution with a 1-hour time step. Detailed introduction is provided in Gelaro et al. (2017).

As explained later in section 3.3, the retrieval of $DAOD_{TIR}$ relies on the difference of brightness temperature (BT) at TOA between the cloud-free clean atmosphere (referred to as "BT_{clean}") and the cloud-free dusty atmosphere (referred as to "BT_{dust}"). Thus, an accurate estimate of BT_{clean} is a prerequisite for the accurate retrieval of $DAOD_{TIR}$. In this regard, the algorithms based on hyperspectral observations have an obvious advantage, i.e., they can select channels in atmospheric window bands to reduce the impacts of atmospheric profile uncertainties. In contrast, the much broader spectral response of IIR bands makes them more susceptible to atmospheric profile uncertainties. To understand the magnitude and impacts of this uncertainty, we performed a careful radiative closure benchmark study. First, we used the "cloud-free clean" scene type in the "CAL_IIR_L2_Track" product to select those cloud-free and low-aerosol-loading profiles. Ideally,

without the impact of cloud or aerosol, the simulated BT_{clean} based on MERRA-2 atmospheric profiles and FASDOM should agree with the observed BT_{clean}. Of course, they could differ significantly in reality because of various uncertainties, including instrument noise, uncertainty in MERRA-2 profile, and/or radiative transfer error. Therefore, the difference between simulated and observed BT_{clean} provides us a reasonable estimate of the impacts of these critical uncertainty sources on our dBT LUT. The results from this radiative closure study are shown in Figure 1.

The radiative closure over land has a large discrepancy (up to ±10 K) because of the high-varied surface emissivity and skin temperate around the TIR window spectrum over bright deserts (Zhou et al. 2013). Thus, in this study, we only consider retrieval over the ocean and mask the land regions. In addition, to focus on the simulation performance over the dust-concentrated region, the derived 2-year annual CALIOP DAOD at 532 nm (referred to as "$DAOD_{532nm}$"; the derivation process is explained in section 3.2) from 2007 to 2008 is used to define the area with noticeable dust loadings for the radiative closure testing. As shown in Figure 1a, the area with DAOD larger than 0.03 is defined as the dust-concentrated region over oceans.

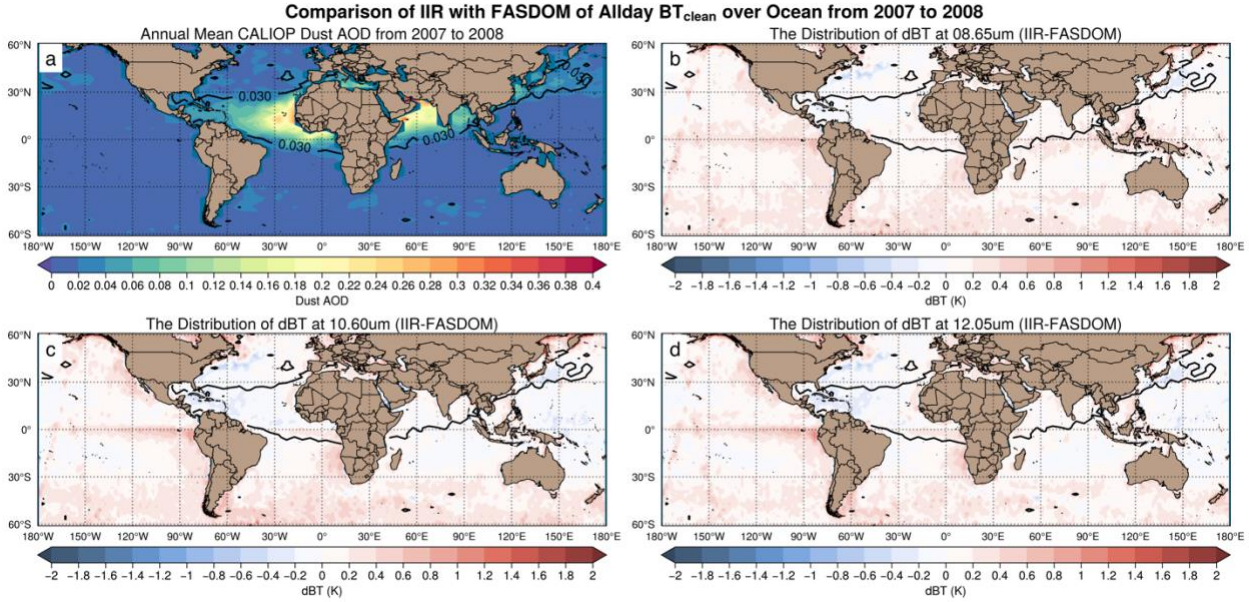

Figure 1 The global distribution of the annual mean CALIOP DAOD (a), the BT_{clean} difference of all-day dBT_{clean} (IIR-FASDOM) at 8.65 μm (b), 10.60 μm (c) and 12.05 μm (d) over oceans from 2007 to 2008. The black contour line represents the annual mean CALIOP DAOD of 0.03 from 2007 to 2008.

Figures 1b, 1c and 1d show the BT_{clean} difference between IIR and FASDOM (referred to as "dBT_{clean}") is within ± 2.0 K at all three IIR bands. Out of the dust-concentrated region, the dBT_{clean} has a positive bias, especially in the Southern Ocean. Although the cause of this bias is not fully understood, it could be a combination of several other factors, including biases in MERRA-2 data and/or issues in radiative transfer models. However, the radiative closure results over the dust-concentrated region are highly encouraging, i.e., with the annual mean difference primarily within ± 0.1 K, indicating a good agreement between simulated and observed BT_{clean}. Figure 2 provides a more quantitative perspective by separating the daytime and the nighttime cases over the dust-concentrated region. As shown in Figure 2b, the probability distribution function (PDF) of dBT_{clean} over the dust-concentrated region for all three IIR bands follows a Gaussian-shape distribution for nighttime cases with the peak centered around zero (biases smaller than 0.05 K). However, the daytime cases in Figure 2a have a 0.25 K positive bias and ~0.15 K larger standard deviations. Similar bias in daytime is found and discussed in previous studies for both IIR and MODIS (Garnier et al. 2021; Garnier et al. 2017). The possible reason of the slight but systematic bias in daytime cases remains unclear if it is due to the IIR-CALIOP's cloud-free clean masking or other reasons. Accordingly, we only use nighttime observations for the $DAOD_{TIR}$ retrieval in this study. Note that the random error of IIR measurement with 0.2 K is already included throughout the radiative closure benchmark. Therefore, the uncertainty from both observations and forward simulations can be represented by one standard deviation of the BT_{clean} difference at each IIR channel.

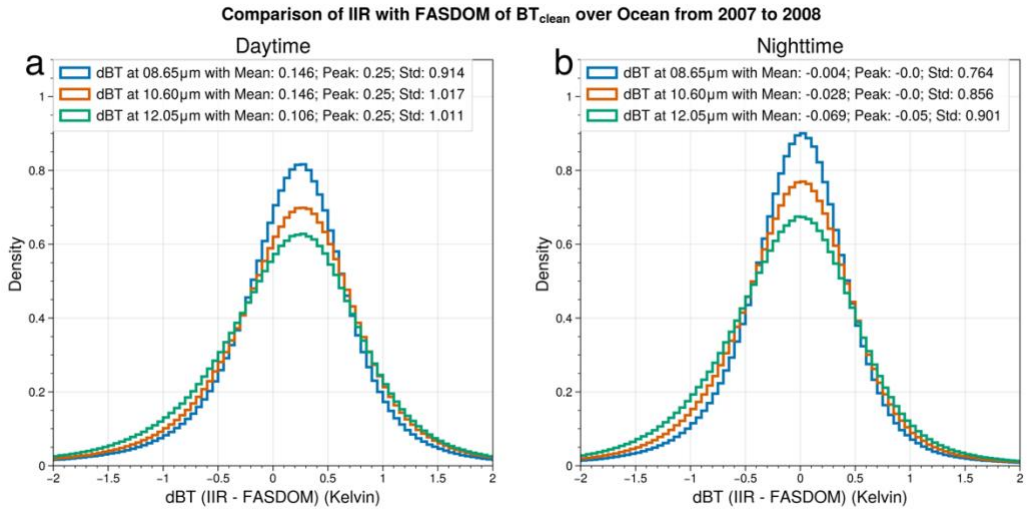

Figure 2 The probability distribution function (PDF) of daytime (a) and nighttime (b) dBT (IIR-FASDOM) of BT_{clean} at 8.65 μm, 10.6 μm and 12.05 μm over oceans from 2007 to 2008 for the dust-concentrated region as indicated in Figure 1.

3. Description of Retrieval Algorithm

3.1 The use of 10.6 μm channel for $DAOD_{TIR}$ retrieval over ocean

Although IIR has three bands with similar observational uncertainties as analyzed above, we choose to use only the 10.6 μm channel for the $DAOD_{TIR}$ retrieval over oceans during nighttime based on the following considerations. First of all, as will be shown later in Figure 5 (section 3.3), as well as in the atmospheric transmission spectrum (Dubuisson et al. 2005), the 10.6 μm channel contains a more extensive dust extinction and with higher atmospheric transmission than the other two channels, which means a better signal-to-noise ratio for the $DAOD_{TIR}$ retrieval. Secondly, as previous studies usually report the $DAOD_{TIR}$ retrieval results at around 10 μm (Capelle et al. 2014; Peyridieu et al. 2010), the choice of 10.6 μm channel will help us compare the result with these previous estimates. Finally, although the three IIR channels provide independent observations, they share similar BT differences due to the change of DAOD at their spectral range (see Figure

A4 in Capelle et al. (2014)), leading to insufficient information content regarding the spectral BT difference among the three IIR channels. Note that we can use a single channel to retrieve the $DAOD_{TIR}$ because CALIOP specifies the vertical distribution of dust. In contrast, hyperspectral IR observations need information at different wavelengths to simultaneously retrieve $DAOD_{TIR}$ and mean dust altitude as the dust layer height has the same order-of-magnitude of information content as $DAOD_{TIR}$ (Klüser et al. 2015; Pierangelo et al. 2004).

If on one hand the use of a single channel makes the $DAOD_{TIR}$ retrieval algorithm relatively straightforward, on the other it requires making more careful assumptions on dust properties, such as their size, shape and complex refractive index. Although this is a common practice in aerosol remote sensing due to the lack of information, the pre-assumed properties inevitably fall short of the variability of actual dust and therefore may lead to retrieval uncertainties. We test the sensitivity of the pre-assumed dust particle size and complex refractive index in our retrieval and analyze their contribution to retrieval uncertainties in sections 3.5 and 3.6. In future research, we will also explore the possibility of retrieving other dust properties in addition to $DAOD_{TIR}$ using more IIR channels and/or other IR observations from, for example, MODIS and AIRS.

3.2 Cloud masking and dust detection

An essential prerequisite for a successful $DAOD_{TIR}$ retrieval is reliable identification of cloud-free and dust-laden profiles and pre-knowledge of the vertical distribution of dust within the profile. This step of cloud masking and dust detection can be challenging for passive sensors with relatively coarse spatial resolution (e.g., AIRS and IASI). But the unique capabilities of CALIOP, together with the supplementary information from IIR, make this step relatively straightforward, as explained below.

We use the 5-km “CAL_LID_L2_05kmAPro” product from CALIOP and the 1-km “CAL_IIR_L2_Track” product from IIR. As aforementioned, the 5-km CALIOP segments are first collocated with the 1-km IIR pixels such that each CALIOP profile contains five IIR pixels.

Cloud screening is done in two steps using the two collocated products. In the first step, we use the vertical features mask ("Atmospheric_Volume_Description") from the "CAL_LID_L2_05kmAPro" product to filter out any 5-km profiles that contain cloud layers or stratospheric aerosol. It should be noted that even after the first step screening, ~59% of the remaining CALIOP 5-km segments are still partly cloudy (i.e., containing sub-pixel clouds, see Table 2). It results from the “hiding” single-shot cloud in the 5-km CALIOP segments. Therefore, in the second step of cloud masking, we use the “Was_Cleared_Flag_1km” to find the cloud-free 1-km IIR pixels within those partly cloudy 5-km CALIOP pixels and assign them pre-quality assurance (pre_QA) flags with discerptions in Table 2. Note that post-quality assurance (post_QA) flags are also assigned for the retrieval result, explained in section 3.6.

After cloud masking, the next step is to identify dust and specify its vertical profile. As the first step of dust detection, we use the extinction control flag (“Extinction_QC_Flag_532”) in the CALIOP product to select only reliable retrievals (i.e., Extinction_QC_Flag_532 =0, 1, 16 or 18 (Winker et al. 2013; Yu et al. 2015)). Then, we further select from the remaining profiles those with the cloud-aerosol discrimination (CAD) score between -100 and -90 to ensure the profile is confidently aerosol (Liu et al. 2009; Yu et al. 2010).

Table 2 The pre- and post-quality control flags assigned in the retrieval process.

QA flag	Value	Description	Number of Samples in 2013 (Total: 1888273)
pre_QA	0	All 1-km pixels in a 5-km profile are cloud-free aerosol	767040 (40.62%)
	1	Part of 1-km pixels in a 5-km profile are cloud-free aerosol	828445 (43.87%)
	2	None of 1-km pixels in a 5-km profile are cloud-free aerosol	292788 (15.51%)
post_QA	0	retrieved DAOD / CALIOP DAOD < 2.0	1796767 (95.16%)
	1	retrieved DAOD / CALIOP DAOD >= 2.0	59013 (3.12%)
	2	A 5-km profile with dBT ($BT_{dust} - BT_{clean}$) > 0	32493 (1.72%)

As mentioned in section 2.1, the extinction profile classified as dust, polluted dust and dusty marine from the V4 CALIOP operational product contains the dust mixture with other non-dust aerosols, such as air pollution and marine aerosols. Because of their small size, these aerosols have very little extinction in the TIR region, even though they have a notable contribution to the visible extinction.

For our $DAOD_{TIR}$ retrieval, we need to know the vertical profile of only dust aerosols. For this purpose, we apply a widely used technique to first derive a vertically resolved fraction of dust backscatter (β_d) to total backscatter (β), i.e., $f_d(z) = \beta_d(z)/\beta(z)$ from the following equation:

$$f_d(z) = \frac{(\delta(z)-\delta_{nd})(1+\delta_d)}{(1+\delta(z))(\delta_d-\delta_{nd})} \quad (1)$$

where δ_d and δ_{nd} are the pre-assumed particulate DPR of dust and non-dust aerosols. Following Yu et al. (2015), the lower and upper limits of δ_{nd} are set to 0.02 and 0.07 and δ_d to 0.20 and 0.30, respectively. The f_d upper bound is estimated based on the combination of $\delta_d = 0.2$ and $\delta_{nd} = 0.02$ and the lower bound based on $\delta_d = 0.3$ and $\delta_{nd} = 0.07$. The value of f_d is set to be 1 when $f_d > 1$ and 0 when $f_d < 0$. For simplicity, the final f_d is set to the mean value of the upper and lower bounds. Lastly, using the derived f_d and pre-assumed lidar ratio for pure dust. i.e., $S_d = 44$

sr at 532 nm, we convert the aerosol backscatter profile ($\beta(z)$) from the CALIOP aerosol profile product to dust extinction profile $\sigma_d(z) = S_d \cdot f_d(z) \cdot \beta(z)$)), and further the $DAOD_{532nm}$ from the column σ_d. It is important to note that the $\sigma_d(z)$ is used for scaling the input layer OD with a given $DAOD_{TIR}$ in FASDOM to represent the vertical distribution of dust. In other words, the assumption of S_d is irrelevant on the $DAOD_{TIR}$ retrieval but impacts the absolute value of $DAOD_{532nm}$. Moreover, we assume that the dust properties, e.g., size and refractive index, are the same within a dust layer. This assumption can lead to uncertainties as dust particles can become stratified during transport because of vertical sedimentation processes (Yang et al. 2012). We leave the investigation of this uncertainty to future research and assume it is a second-degree level compared to other sources, e.g., radiative transfer uncertain, dust size and dust refractive index.

The corresponding cloud-free 1-km IIR BTs are eventually averaged back to 5 km footprints. For example, if a partly cloudy 5-km CALIOP pixel has three cloud-free 1-km IIR pixels, then the input BTs for the $DAOD_{TIR}$ retrieval is based on the mean value of the three cloud-free IIR pixels. The retrieval results are, therefore, in 5 km spatial resolution along the CALIOP track.

3.3 A priori assumption of dust optical properties

The single band (i.e., 10.6 μm) $DAOD_{TIR}$ retrieval requires dust properties other than the dust altitude to be pre-assumed. This section introduces the dust particle size distribution (PSD), dust shapes, and dust complex refractive index (RI) that are used to derive the dust bulk scattering properties, including the extinction efficiency (Q_{ext}), single-scattering albedo (SSA) and asymmetry factor (g-factor).

As the retrieval is implemented over oceans only, it needs appropriate a priori dust PSDs obtained at dust-transport areas. Hence, we retrieve and report two sets of $DAOD_{TIR}$ retrievals based on two pre-assumed dust PSDs; as introduced further below, one is retrieved by AERONET measurements at Cape Verde (Dubovik et al. 2002), and the other is observed during the Fennec 2011 aircraft campaign (Ryder et al. 2013b). Song et al. (2018) used these two dust PSD to evaluate dust DRE over the tropical North Atlantic. Their result shows a remarkable difference of simulated DRE_{LW} based on these two PSDs. Without the observational record in TIR, it is reasonable to have distinguished extrapolated $DAOD_{TIR}$ and, therefore, DRE_{LW} based on the same $DAOD_{VIS}$ but different PSDs, especially in the coarse mode. Therefore, it is worth showing if similar impacts of dust particle size occur on the $DAOD_{TIR}$ retrieval.

The first PSD is based on AERONET climatology at Cape Verde (16°N,22°W) (referred to as "AERONET" PSD) averaged from 1993 to 2000 by Dubovik et al. (2002) to represent the transported dust PSD as it is from a dust-dominant site (Gama et al. 2015; Mahowald et al. 2014; Song et al. 2018). Note that the PSD retrieval artifact of AERONET measurements due to dust non-sphericity was corrected in our use of the AERONET PSD (Dubovik et al. 2002). Details of the AERONET PSD retrieval process can be found in Dubovik et al. (2000). The second set of dust PSD is taken from the Fennec field campaign during June 2011 over the eastern Atlantic Ocean, which is categorized as the airborne dust within the Saharan Air Layer (SAL) (referred to as “Fennec” PSD). This category is from the average of vertical profile observations excluding the marine boundary layer. It represents the airborne dust transported over the nearby eastern Atlantic Ocean with the remarkably disclosed larger particle sizes than measured previously in dust layers, as well as the AERONET PSD (see Figure 3). The errors due to sizing uncertainties have also explicitly been quantified (see Ryder et al. (2013a) for full details).

Figure 3 shows the size-normalized volume size distribution of AERONET PSD and Fennec PSD as the visual comparison. The coarse mode of AERONET PSD has the peak with diameter around 3 μm, while the diameter of the peak of Fennec PSD is larger than 10 μm. As the fine-mode PSD rarely (~10%) changes the dust extinction in TIR (Pierangelo et al. 2013), the difference of the coarse mode between the two PSDs mainly impacts the $DAOD_{TIR}$ retrieval.

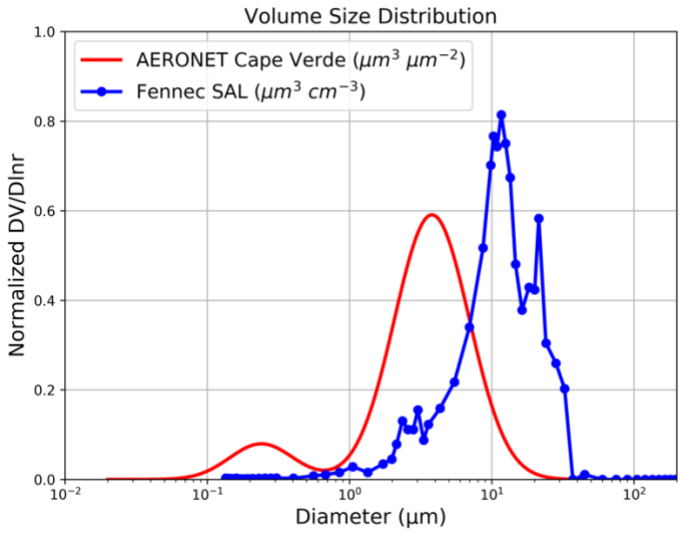

Figure 3 The size-normalized dust volume PSD. The red curve represents the PSD retrieved from AERONET measurements at Cape Verde reported in Dubovik et al. (2002). The blue dot curve represents the PSD obtained from airborne measurement during Fennec campaign during June 2011 over the eastern Atlantic Ocean (Ryder et al., 2013a).

For the dust RI, we use a state-of-art database developed by Di Biagio et al. (2017) (referred to as "Di-Biagio" database). It has laboratory-measured RIs for dust aerosols generated from natural soil samples collected in 19 arid and semi-arid sites from 8 regions globally, including northern Africa, the Sahel, eastern Africa and the Middle East, Eastern Asia, North and South America, southern Africa, and Australia. Compared with other older dust RI databases in the literature, e.g.,

Volz (1973) and OPAC (Hess et al. 1998), the Di-Biagio database is more comprehensive and allows for the choice of regional dependent RI for $DAOD_{TIR}$ retrieval. As shown in Figure 4, in our algorithm, we divide the global ocean into seven regions and then assign one or more regional RI from the Di-Biagio database based on the dust transport model simulations (Griffin 2007; Querol et al. 2019). For each 5-km IIR pixel, we take the ensemble of RI for the region of influence and average the retrieved $DAOD_{TIR}$ corresponding to each assigned RI. Although this is a somewhat crude way, it still helps us capture the variability of dust RI to a certain extent. Moreover, as explained in section 3.4, the sensitivity of regional RIs to the radiative signal of dust at the IIR 10.6μm channel is relatively low.

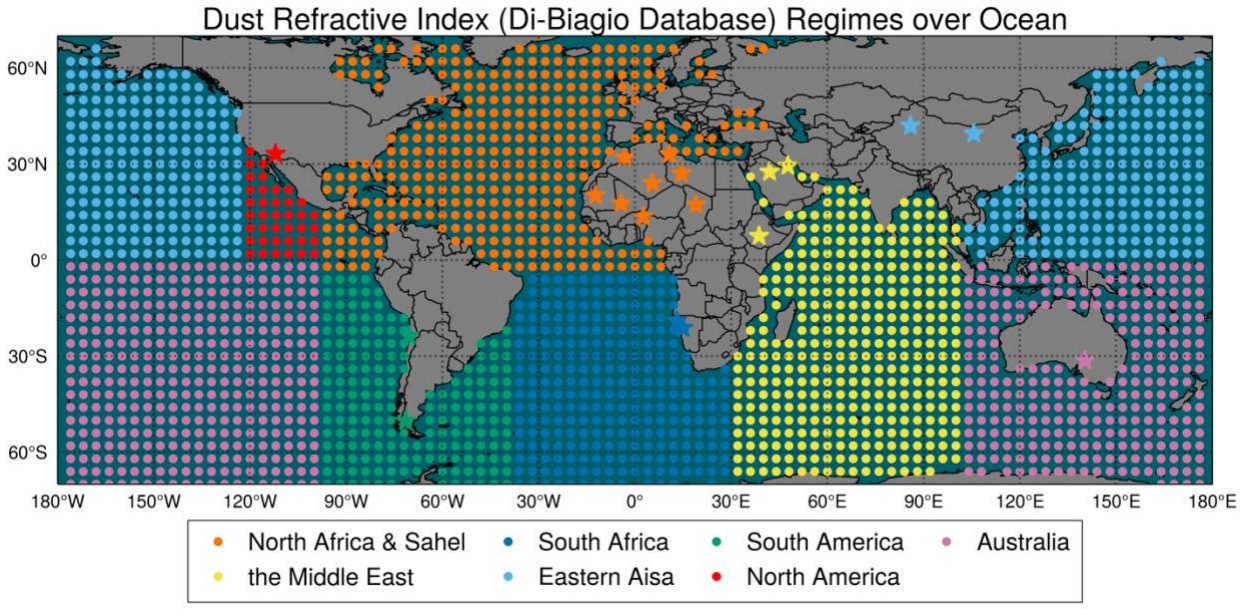

Figure 4 The assigned eight ocean regimes corresponding to Di-Biagio RIs according to the dust transport simulation in Querol et al. (2019). The stars over land represent the location of the soil and sediment samples collected for the dust RIs. Each color of the stars represents the regime for which it applies.

For dust shape, studies on their impact on scattering properties have proved that spheroid assumption is a reasonable first-order approximation of the shape of non-spherical dust (Dubovik

et al. 2006; Mishchenko et al. 1997). Consequently, we assumed a spheroid shape of dust particles with the size-independent aspect ratio distribution from Dubovik et al. (2006).

Dust bulk scattering properties (i.e., Q_{ext}, SSA and g-factor) for the different combinations of dust PSDs, RIs and shapes are calculated using the T-matrix code developed by Mishchenko (2000) as shown in Figure 5. We also calculate the $Q_{ext,TIR}/Q_{ext,VIS}$ (i.e., TIR/VIS) ratio as it is not only the key element to compare $DAOD_{TIR}$ retrievals with observations in VIS (e.g., CALIOP DAOD; see section 4.1) but also impacts the DRE_{LW} calculation in climate models (Capelle et al. 2014; Kok et al. 2017). Because the variability of the real part of SW RIs in literature data is negligible at 550 nm (Ryder et al. 2019), we use one SW RI (1.53-0.002i at 550 nm) from the OPAC database to calculate the $Q_{ext,VIS}$ with the given dust PSDs.

In the plots, red and blue color groups correspond to scattering properties based on AERONET and Fennec PSD, respectively. Each color group contains 19 lines corresponding to the 19 RI in the Di-Biagio database. By looking at the difference between two dust PSD groups using the Di-Biagio RIs, one can see, in Figure 5a, 5b and 5d, that the sensitivity of dust size to Q_{ext}, TIR/VIS ratio and g is more significant than that of dust RIs as the groups are completely separated, while the spectral variation of SSA in Figure 5c in two groups are more entangled. It is because the regional RIs mainly differ in the imaginary parts, while the real parts are almost identical at 10.6 μm (Di Biagio et al. 2017). However, the change of SSA with RI shows a limited impact on the radiative signal of dust, which is discussed in section 3.4. The grey and black bars in Figure 5 are the SRF (dash lines with right y-axis) integrated scattering properties centered at 3 IIR bands. The integrated SSA and g-factor of dust at 10.6 μm by IIR SRFs are finally used as the input of dust radiative properties in the FASDOM simulation for retrieving $DAOD_{TIR}$.

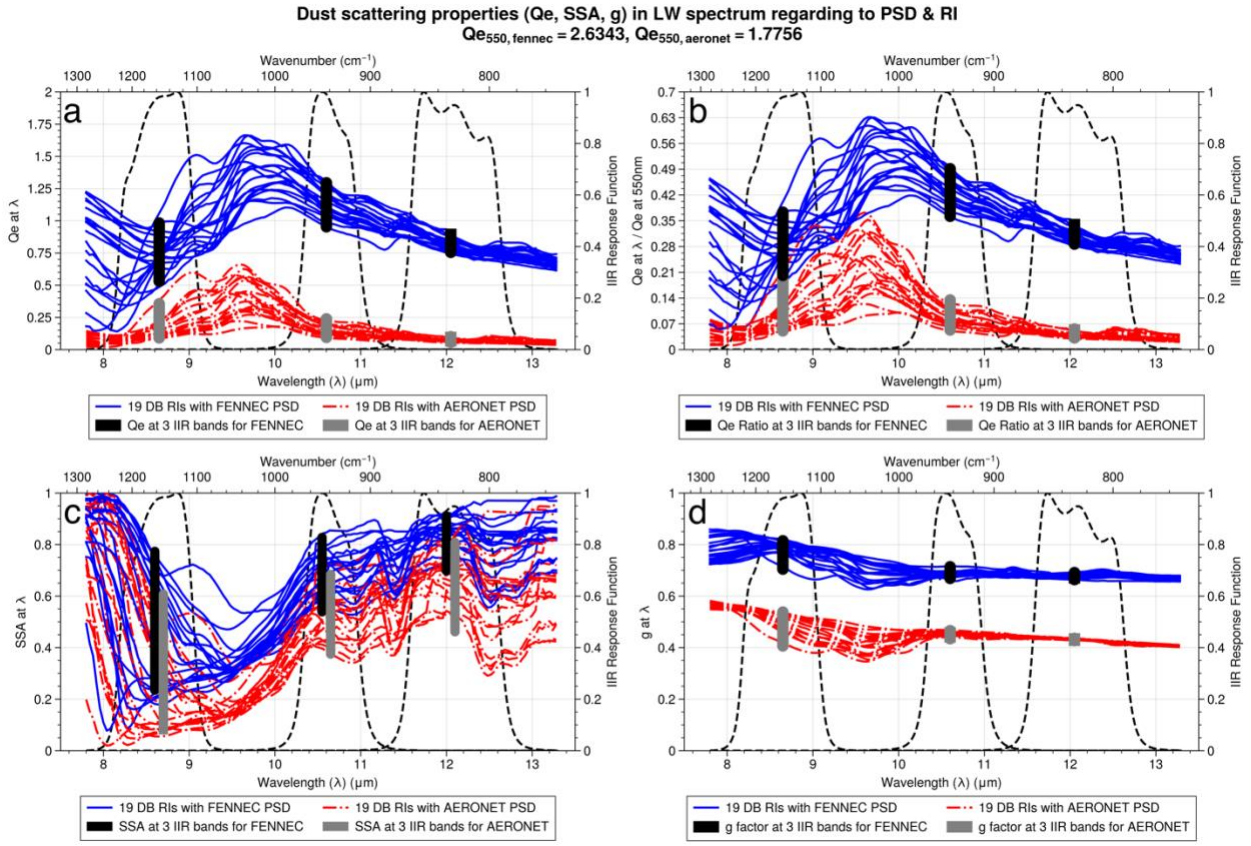

Figure 5 The scattering properties (Qext (a), Qext ratio (b), SSA (c) and g (d)) calculated using the spheroid assumption by T-matrix. The blue lines and red dash-dot lines represent the result calculated by assuming the Fennec PSD and the AERONET PSD, respectively. Black and grey bars represent the convolved scattering properties using the IIR spectral response functions (SRF) (dash lines with right y-axis) at three bands, respectively (centered at 8.65, 10.6 and 12.05 μm).

3.4 The Retrieval framework

A flow chart of our $DAOD_{TIR}$ retrieval algorithm is given in Figure 6. With the IIR BT at 10.6 μm for the identified cloud-free dust profiles after the screening process introduced in section 3.2, the BT difference due to dust (referred to as "dBT") is then obtained by subtracting the IIR observed BT_{dust} with the FASDOM simulated BT_{clean} using the collocated MERRA-2 assimilated atmospheric profiles (included temperature, water vapor and ozone profiles with height and

pressure profiles) and surface properties (included MERRA-2 surface temperature and surface emissivity from IIR Level-2 product). Afterward, with the a priori dust scattering properties calculated based on the assigned regional RIs, dust PSD and shape, and the CALIOP-derived dust vertical distribution, the look-up table (LUT) of dBT as a function of $DAOD_{TIR}$ is built simultaneously for each cloud-free dust profile. Finally, the corresponding $DAOD_{TIR}$ to the matched BT from LUT with the observational IIR BT can be retrieved. The following estimated absolute retrieval uncertainty and the post-filtering process are introduced in section 3.6.

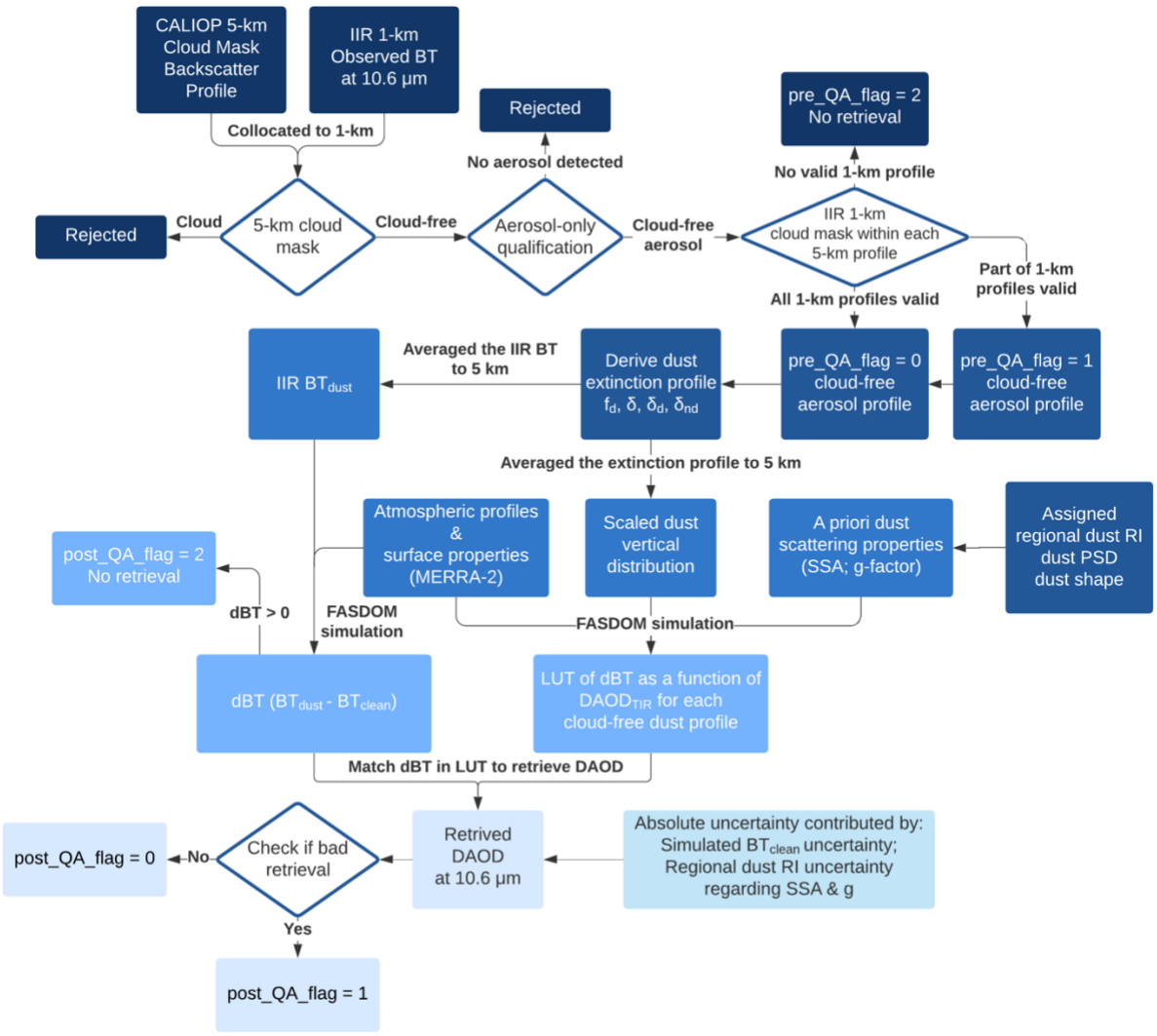

Figure 6 Flowchart of the IIR-CALIOP $DAOD_{TIR}$ retrieval algorithm.

As an illustrative example, we first applied the retrieval framework to a case in Figure 7. In Figure 7a, CALIOP observations reveal a dense dust layer from 3 km to 5 km above the ocean surface with some broken marine boundary layer clouds underneath it. Figure 7b shows the variation of IIR observed BT_{dust} at 10.6 μm and the corresponding BT_{clean} simulated by FASDOM. In this case, the 1-km IIR pixels can capture BT's rapid change due to the marine boundary layer cloud extinction. After applying the dust detection method presented in section 3.2, the identified cases maximally exclude the observed BT with cloud contaminations (blue dots on top of IIR BT in Figure 7b). Corresponding to the cloud-free dust cases, Figure 7c shows the comparison of dBT (IIR BT_{dust} - FASDOM BT_{clean}) with the derived CALIOP DAOD at 532 nm. Evidently, the IIR dBT has a negative correlation with the CALIOP DAOD for this scene, illustrating the sensitivity of IIR observation to the $DAOD_{TIR}$ retrieval at 10.6 μm. Because the case's location is in the North Atlantic affected by the Africa and Sahel regions in Figure 4, we use the dust RIs from Sahara and Sahel accordingly, in the calculation. Afterward, both Fennec PSD and AERONET PSD are used to obtain two sets of dust bulk scattering properties for the retrieval. Utilizing the dBT signal, Figure 7d shows the retrieved DAOD at 10.6 μm (referred to as "$DAOD_{10.6\mu m}$") for the dust with AERONET PSD (red dot line) and Fennec PSD (blue dot line). We found that the same dBT signal yields larger retrieved DAOD when using Fennec PSD's larger particle size than AERONET PSD. The explanation on this requires further understanding about the impact of bulk scattering properties regarding different dust PSD on the dBT signal, which is discussed in the next section.

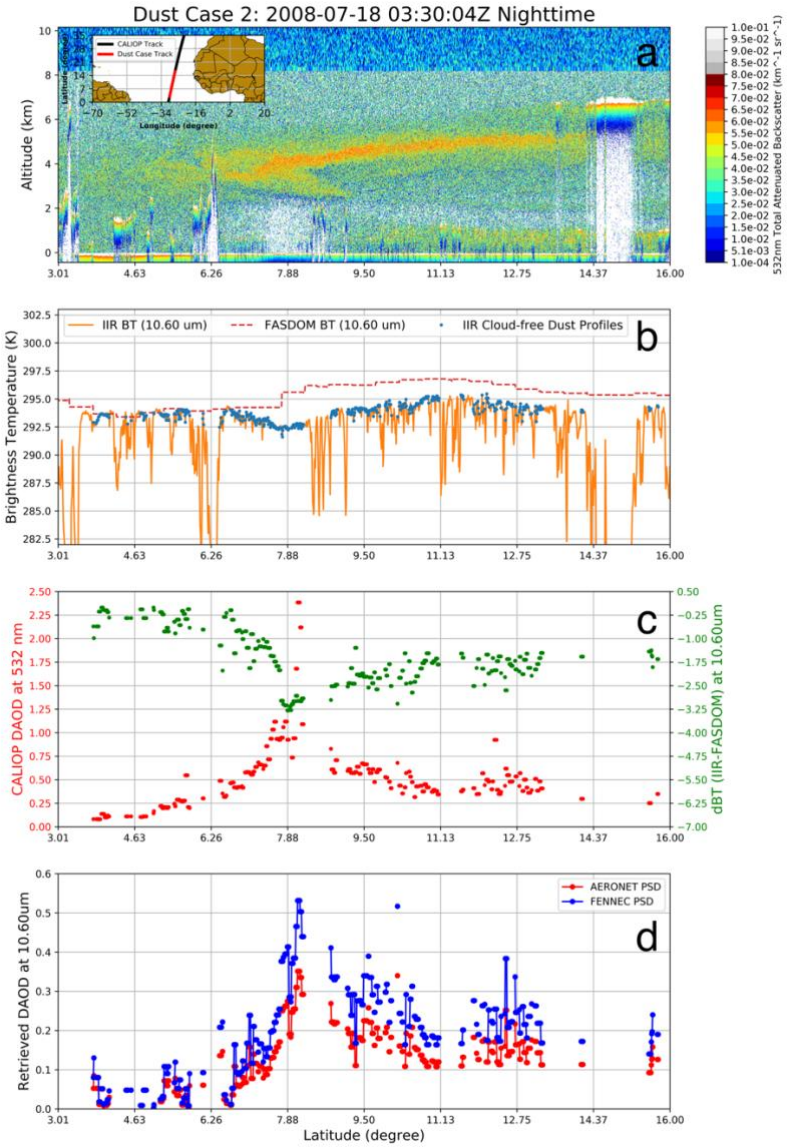

Figure 7 a) The CALIOP total attenuated backscatter at 532 nm on July 18th, 2008, in Tropical North Atlantic (the orbit at upper left). b) The IIR BT_{dust} at 10.6 μm (orange lines) and the FASDOM BT_{clean} at 10.6 μm (red dash lines), respectively. c) The dBT (IIR-FASDOM) (green dots) and the CALIOP DAOD (red dots) of cloud-free dust-laden profiles corresponding to the left and right y-axis, respectively. d) The retrieved $DAOD_{10.6\mu m}$ using Fennec PSD (blue lines) and AERONET PSD (red lines).

3.5 Sensitivity of the retrieval to assumed dust particle size and dust refractive indices

In FASDOM simulation, the variation of the input SSA and g-factor due to the change of dust PSD and RI yields different simulated BT_{dust}, hence, different dBT LUT. In the retrieval framework, with the same observed dBT, the change of LUT leads to different retrieved DAODs corresponding to the change of dust PSD and RI. Therefore, investigating how dust PSD and RI impact the dBT simulation by changing the dust scattering properties (see Figures 5c and 5d) helps understand the $DAOD_{TIR}$ retrieval uncertainty caused by the pre-assumed dust properties. The dBT simulation also depends on the atmospheric states, the surface properties, and the dust vertical distribution. To evaluate that, we study the sensitivity of dBT at IIR 10.6 μm channel for two selected cases. One is collected over the sub-tropical Atlantic Ocean (Figure 8b), the other is observed at the coastal region near the Sahara Desert (Figure 8e). Table 3 lists the parameters of the two cases in the sensitivity studies.

Table 3 Parameters in the sensitivity study for the selected cases.

Time	Geolocation	Surface temperature	Surface emissivity at 10.6 μm	Integrated water vapor path	Simulated BT_{clean}	Input $DAOD_{TIR}$
2008-07-18 03:30:04 UTC	7.5N, 28.75W	301.462 K	0.984	5.510 g/cm^2	295.612 K	0.2
2006-07-01 03:03:34 UTC	16.5N, 20.625W	296.672 K	0.984	2.722 g/cm^2	294.853 K	0.2

In the first case, a long-term transport dust layer is observed between about 2.5 km and 6.25 km by CALIOP (Figure 8c), with a layer mean temperature around 270 K compared to the warm surface temperature at 301 K (Figure 8b). In the sensitivity test, we keep the $DAOD_{TIR}$ settled at

0.2 at the 10.6 μm and then use FASDOM to simulate the BT_{dust} and the corresponding dBT (i.e., BT_{dust} minus BT_{clean} (see Table 3) with different combination of SSA from 0 and 1.0 and g-factor from 0 to 1.0. The dBT result is shown as the color contour in Figure 8a. When SSA approaches zero, the scattering effect of dust diminishes, which explains the independence of dBT on the g-factor, and in this case, the dust layer can be regarded as a purely absorbing gas layer. Because the dust layer is much colder than the surface, its absorption effect dominates, leading to a negative dBT around -2K. When SSA attains to unity and g-factor approaches zero (i.e., lower right corner of Figure 8a), the backward scattering effect dominates, and dust emission diminishes. This condition yields the most negative dBT. When both SSA and g-factor approaches to unity (i.e., upper right corner of Figure 8a), although the scattering effect of dust is strong, the scattered direction is forward, which means the emission from the surface can "pass" through the dust layer despite the strong scattering. In this condition, the dust layer appears to be "transparent", and as a result, the dBT is zero.

After understanding how dBT varies with hypothetical SSA and g-factor in this case, we over-plot the "real" SSA and g-factor computed based on a different combination of dust PSDs and RIs (i.e., color lines with dot marker). Each of the eight color lines corresponds to one of the eight RI in the Sahara and Sahel deserts (see Figure 4) in the Di-Biagio database. Each dot marker in a line corresponds to a lognormal dust PSD with an effective radius (re) from 0.4 μm to 7.7 μm with one standard deviation of 0.6 μm. Furthermore, we use the black stars to indicate the scattering properties based on the AERONET PSD and blue stars for the Fennec PSD. When dust size is small, both SSA and g-factor are close to zero. As dust size increases, the SSA first increases faster than the g-factor. But after passing about the size of AERONET PSD, the SSA remains almost invariant for a given RI while the g-factor keeps increasing. For a given dust size, the variation of

RI mainly affects the SSA and has little influence on the g-factor, which is consistent with the discussion in Figure 5. Combining the behavior of line plots and background color contour, one can see that the dBT simulation at 10.6 μm is more sensitive to dust PSD than RI. It also becomes clear that with the same $DAOD_{TIR}$ input, the BT_{dust} simulated based on the Fennec PSD is warmer than that on the AERONET PSD due to the contrast in g-factor. In other words, when retrieving $DAOD_{TIR}$ from the same observed dBT, the retrieved $DAOD_{TIR}$ based on the Fennec PSD is larger than that based on AERONET PSD, as shown in Figure 7d.

In the second case, a dust layer extends from about 6.0 km to 0.5 km but concentrates mostly near the surface. Moreover, there is a temperature inversion (TI) in the upper boundary layer between 0.5 km and 1.25km. Such TI was often observed over the coastal region near the Sahara Desert. It is believed to the result of the warmer Saharan Air Layer overlaying colder Atlantic Ocean surface (Dunion and Velden 2004; Gutleben et al. 2019; Wong et al. 2009). Both the lower altitude and the temperature inversion help enhance the emission effect of dust. As a result, the dependence of dBT on SSA and g-factor in the case (see Figure 8d) is quite different from that in the first case (Figure 8a). In particular, the dependence of dBT on the SSA and, therefore, the choice of RI is significantly stronger due to a more substantial emission effect. It implies that using a pre-assumed RI for $DAOD_{TIR}$ retrieval when the real RI has significant variability could induce larger uncertainty when the dust emission is strong. Fortunately, as discussed later in Section 5, TI is mainly found in the narrow coastal regions of North Africa and the Middle East (Clarisse et al. 2019).

Generally, for the transported dust with the sub-tropical atmospheric states (Figure 8a), the assumed dust PSD dominates the $DAOD_{TIR}$ retrieval uncertainty due to the a priori dust assumption.

The uncertainty due to dust RI assumption should be noticed if the dust emission effect is enhanced by TI, which would occur over the coastal region near dust sources.

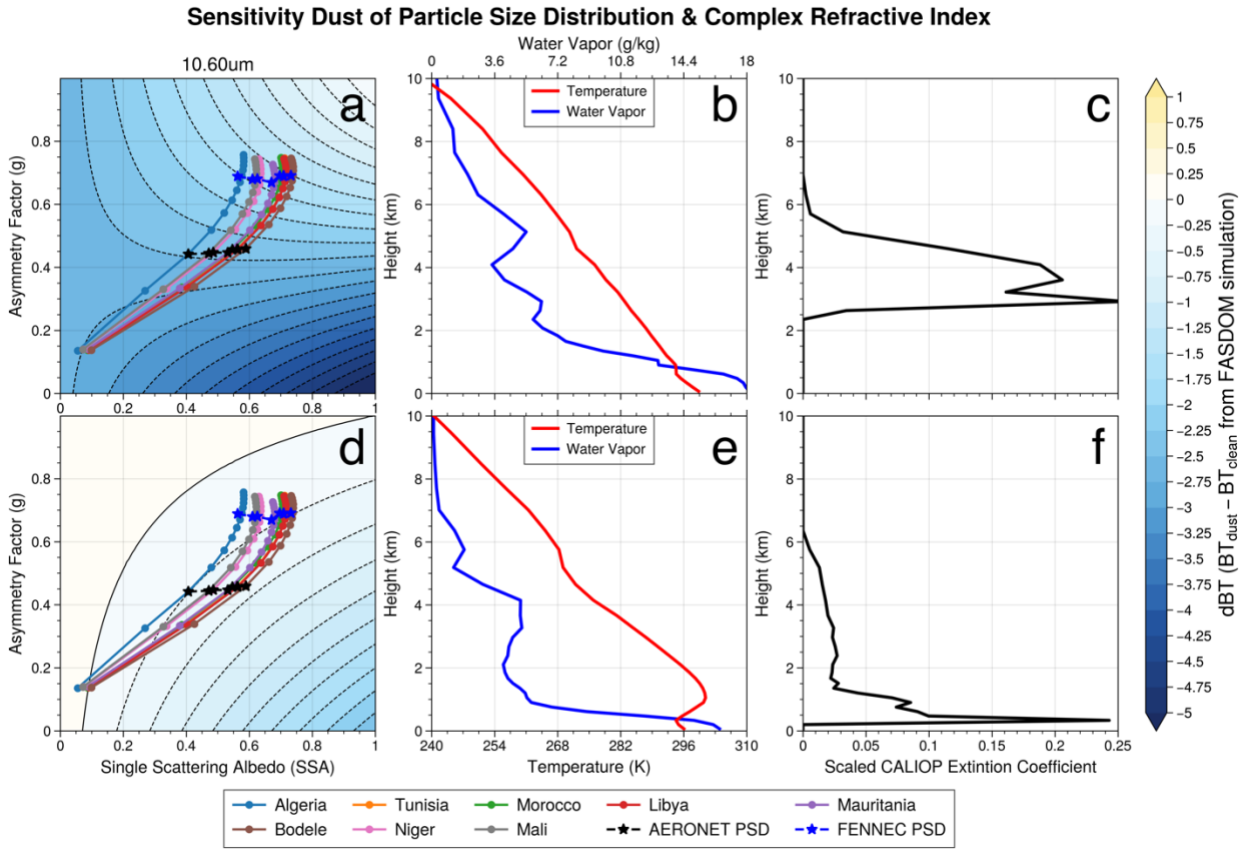

555 Figure 8 (a) and (d) represent the contours of dBT between BT_{clean} and BT_{dust} from the FASDOM simulation at IIR Band 10.6 μm with perturbed g factor (y-axis) and SSA (x-axis) by the given $DAOD_{TIR}$ (value of 0.2) corresponding to the sub-tropical (b) and SAL (e) atmospheric profiles, respectively. (c) and (f) represent the corresponding vertical profiles of dust extinction coefficient with the atmospheric profiles of (b) and (e), respectively. The real and dash contour lines represent positive and negative values of dBT, respectively. The dot lines with color in (a) and (d) represent the g-factor and SSA calculated based on combinations of
560 Di-Biagio RIs in Sahara/Sahel deserts and the perturbed PSDs. Each dot marker in a line corresponds to a lognormal dust PSD with an effective radius (re) from 0.4 μm to 7.7 μm with one standard deviation of 0.6 μm. Stars with dash lines in (a) and (d) represent the g-factor and SSA based on AERONET PSD (black) and Fennec PSD (blue) with corresponding dust RIs.

3.6 Uncertainty analysis and post-filtering

As we separate $DAOD_{TIR}$ retrieval into two sets based on two dust PSDs, the difference between the two retrievals is served as the estimation of uncertainty due to dust size. Apart from this, the uncertainty from observation, atmospheric assumption and a priori dust RI is further quantified for the global retrieval results.

As mentioned in section 2.2, the BT_{clean} difference with a standard deviation, S_{dBT}, can be counted as the combined uncertainty in the instrument, ancillary data (e.g., MERRA-2 profiles), and radiative transfer simulation. For nighttime observations of the IIR 10.6 μm channel over ocean, we use S_{dBT}=0.856 K (as shown in Figure 2b). The influence of the uncertainty in dust RI is decomposed into two parts corresponding to the impacts of dust RI on SSA and g-factor, respectively. Based on these considerations, we propose to use the following equation to estimate the uncertainty in the retrieved DAOD:

$$s_{DAOD} = \sqrt{(\frac{\partial DAOD}{\partial dBT})^2 {s_{dBT}}^2 + (\frac{\partial DAOD}{\partial SSA})^2 {s_{SSA}}^2 + (\frac{\partial DAOD}{\partial g})^2 {s_g}^2} \quad (2)$$

where s_{DAOD} is the absolute uncertainty on the retrieved DAOD, s_{SSA} and s_g are the standard deviation of SSA and g-factor, respectively, which are calculated based on each regional RIs in the corresponding RI regime. The perturbation of dBT is 20% of the observed IIR dBT (i.e., IIR BT_{cdust} – FASDOM BT_{clean}), while the perturbations of SSA and g-factor are the difference between the maximum and minimum values calculated from the regional RIs. The corresponding change of DAOD to the perturbation is then used to obtain $\frac{\partial DAOD}{\partial dBT}$, $\frac{\partial DAOD}{\partial SSA}$ and $\frac{\partial DAOD}{\partial g}$.

The information content of dust with small DAOD or low layer height is generally lower than the uncertainties from the observation and the forward model simulation (Klüser et al. 2015). Hence, for CALIOP DAOD less than 0.05 at 532 nm, the retrieval of $DAOD_{TIR}$ is hardly achievable. These cases are set to be zero for reducing bias.

Figure 9a, and 9b show the mean retrieved $DAOD_{10.6\mu m}$ and mean uncertainty for two-year data from 2013 to 2014. The retrieval uncertainty is as comparably large as the DAOD. Figure 9c shows the histogram of the three propagation terms of uncertainties in Eq. (4). Consistent with the discussion in section 3.5, dust RI contributes only ~10% of in the DAOD uncertainty by the perturbation on SSA and g-factor. About 90% of the uncertainty is from the term of dBT uncertainty, representing the uncertainty from instrumental noise, atmospheric assumptions, and radiative simulations.

Because of the relatively large uncertainties, we alternatively use the synergic CALIOP $DAOD_{532nm}$ to filter the unrealistic retrieval results. As mentioned in section 3.2, the $DAOD_{532nm}$ also contains uncertainties from the a priori dust DPR and LR, which are not evaluated in this study. Based on Figure 5b and precious studies (Song et al. 2018), the ratio of $DAOD_{10.6\mu m}$ to $DAOD_{532nm}$ is most likely smaller than unity. Including the mean retrieval uncertainty, retrievals have a chance to get close to or exceed 100% relative uncertainty. Therefore, as listed in Table 2, we assign post_QA = 1 for results with a ratio $DAOD_{10.6\mu m}$ / $DAOD_{532nm}$ > 2 as they are no longer physically meaningful. We also assign post_QA = 2 for a few unretrievable cases (1.72%) with the simulated BT_{dust} warmer than BT_{clean}. Although it is theoretically possible if a significant temperature contrast between the dust layer and the surface occurs, it also requires a strong dust absorption effect (see Figure 8d), which is hardly achieved by the a priori dust at 10.6 μm. Therefore, we believe that these cases are due to the uncertainty in the observation and/or radiative transfer simulation. In the rest of the paper, the retrieval results are all applied QA flags with pre_QA $\leq$ 1 and post_QA = 0.

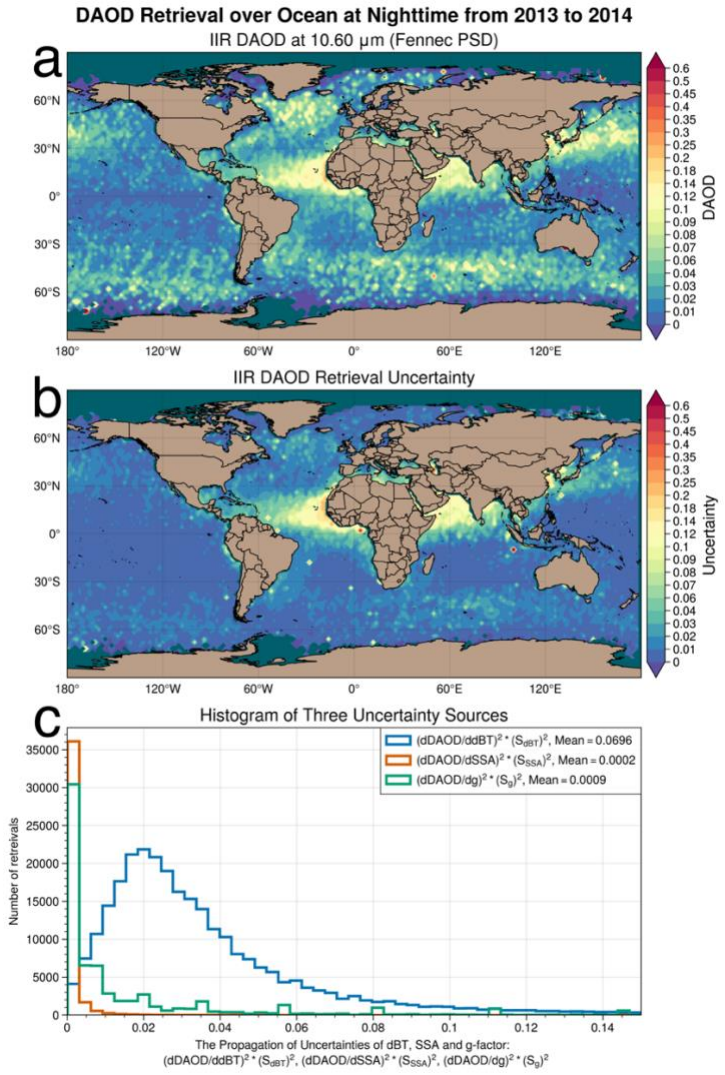

Figure 9 a) The distribution of mean $DAOD_{10.6\,\mu m}$ using Fennec PSD from 2013 to 2014. b) The mean absolute DAOD uncertainty. c) The histogram of three uncertainty propagations ($(\frac{\partial DAOD}{\partial dBT})^2 {s_{dBT}}^2$, $(\frac{\partial DAOD}{\partial SSA})^2 {s_{SSA}}^2$ and $(\frac{\partial DAOD}{\partial g})^2 {s_g}^2$) for retrievals from 2013 to 2014

4. Retrieval results

4.1 Spatial and temporal pattern of DAOD at 10.6um

In this section, we present the climatological $DAOD_{10.6\mu m}$ retrieval results from 2013 to 2017 from our algorithm as explained above. Figure 10 shows the seasonal variation of the retrieved $DAOD_{10.6\mu m}$ based on the AERONET PSDs (left column, referred to as "AERONET $DAOD_{10.6\mu m}$" hereafter) and Fennec PSD (middle column, hereafter "Fennec $DAOD_{10.6\mu m}$"). We also plot the CALIOP $DAOD_{532nm}$ based on the method in Section 3.2 (right column) for comparison purposes. As the retrieval uncertainties of $DAOD_{532nm}$ are not evaluated in this study, instead of focusing on the absolute value of $DAOD_{532nm}$, we use the $DAOD_{532nm}$ as the reference for the seasonal variation patterns of the retrieved $DAOD_{10.6\mu m}$ and the implication of the ratio between VIS (i.e., 532 nm) and TIR (i.e., 10.6 μm). Table 4 shows the seasonal-averaged DAOD retrieved from IIR and CALIOP using AERONET and Fennec PSD. Note that the global average weighted by surface areas excludes the polar region where dust is rarely found. We also highlight regional mean DAODs over four active dust transport regions (i.e., North Atlantic (NA), Tropical Atlantic (TA), Indian Ocean (IO) and Northwest Pacific (NP)) with geolocation range in Figure 10 and Table 4.

Table 4 The seasonal and global/regional mean of all retrieved DAOD from 2013 to 2019

Product	Season	Global (60°S~60°N)	Regions			
			North Atlantic (4°N~34°N, 90°W~0°)	Tropical Atlantic (10°S~4°N, 54°W~14°E)	Indian Ocean (0°~30°N, 40°E~70°E)	Northwest Pacific (14°~56°N, 120°E~180°)
IIR AERONET $DAOD_{10.6\mu m}$	Spring	0.007	0.020	0.025	0.045	0.013
	Summer	0.008	0.036	0.007	0.069	0.002
	Autumn	0.005	0.015	0.007	0.032	0.003
	Winter	0.004	0.012	0.032	0.017	0.007
	Annual	0.006	0.021	0.018	0.040	0.006

IIR Fennec $DAOD_{10.6\mu m}$	Spring	0.009	0.031	0.034	0.066	0.017
	Summer	0.011	0.055	0.009	0.116	0.002
	Autumn	0.006	0.021	0.008	0.044	0.004
	Winter	0.005	0.017	0.045	0.022	0.008
	Annual	0.008	0.031	0.024	0.062	0.008
CALIOP $DAOD_{532nm}$	Spring	0.026	0.066	0.073	0.128	0.038
	Summer	0.030	0.105	0.029	0.251	0.012
	Autumn	0.020	0.044	0.027	0.078	0.017
	Winter	0.020	0.044	0.100	0.055	0.024
	Annual	0.024	0.065	0.057	0.128	0.023
IASI-ULB $DAOD_{10.0\mu m}$	Spring	0.003	0.020	0.018	0.035	0.012
	Summer	0.003	0.044	-0.001	0.070	-0.004
	Autumn	-0.002	0.008	-0.007	0.011	-0.008
	Winter	-0.001	0.005	0.019	0.004	-0.001
	Annual	0.001	0.019	0.007	0.030	-0.001
IASI-LMD $DAOD_{10.0\mu m}$	Spring	0.027	0.048	0.047	0.080	0.022
	Summer	0.032	0.096	0.019	0.185	0.028
	Autumn	0.021	0.040	0.016	0.041	0.017
	Winter	0.024	0.027	0.043	0.029	0.013
	Annual	0.026	0.053	0.031	0.084	0.020

In spring, the outflow of Asian dust to NP is seen from $DAOD_{532nm}$. Both AERONET and Fennec $DAOD_{10.6\mu m}$ capture this pattern. However, the $DAOD_{10.6\mu m}$ decreases fast eastward of 180°W while the CALIOP DAOD is still noticeable even around the west coast of the U.S. A possible reason is that the large dust particles deposit to the ocean during transport, leading to a reduction of both dust size and total AOD, and therefore a reduced signal for the TIR retrieval. In summer, the $DAOD_{10.6\mu m}$ captures the outbreaks of dust transport from Sahara and Sahel to NA,

with averaged values ranging from 0.03 to 0.06. Meantime, dust over IO is transported from the Middle East and/or Sahara source regions, which has an average DAOD from 0.07 to 0.12. In autumn, the dust transport over NA, IO, and NP is weakened compared to summer. In winter, the south-shifted trade wind in the northern hemisphere drives more dust transport to TA than NA. We find the highest $DAOD_{532nm}$ (~0.1) and $DAOD_{10.6\mu m}$ (0.03 ~ 0.04) over TA in winter compared with other seasons. Meanwhile, dust has more chance to mix with smoke and biomass burning aerosols emitted from Tropical Africa. The mean $DAOD_{532nm}$ in winter over TA shares a similar average value (~0.1) with that in summer over NA, while the mean $DAOD_{10.6\mu m}$ in winter over TA is lower than that (0.04 ~ 0.05) in summer over NA, implying a reduced TIR signal due to the lower fraction of dust in the mixture during the transport to TA.

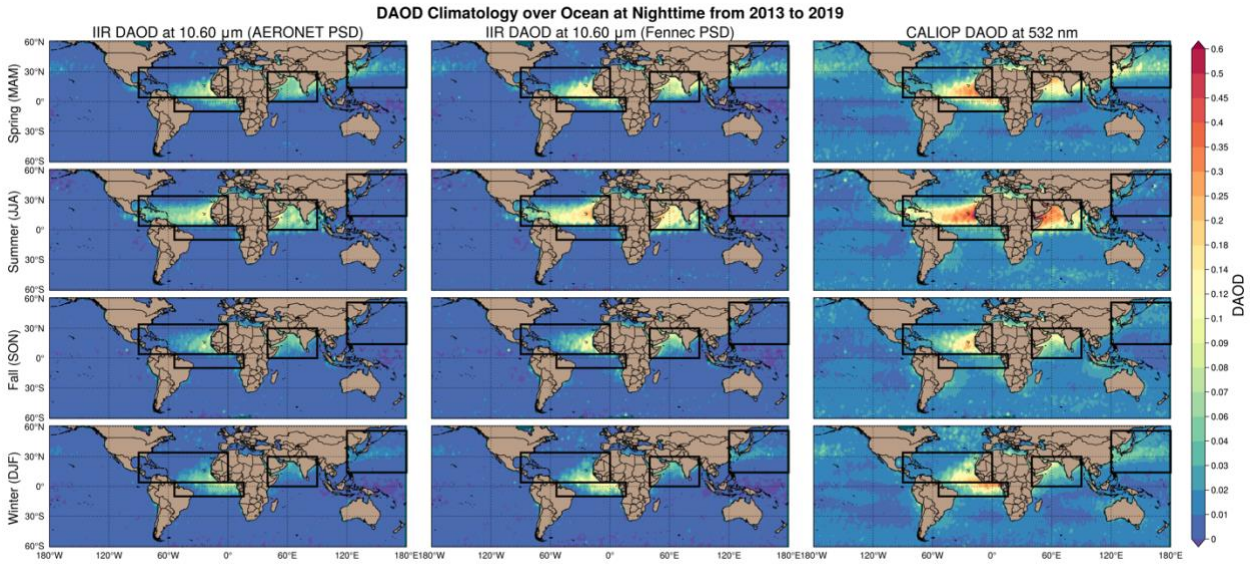

Figure 10 The global distribution of seasonal averaged $DAOD_{10.6\ \mu m}$ based on AERONET PSD (left columns) and Fennec PSD (middle columns) and CALIOP $DAOD_{532\ nm}$ (right columns) from 2013 to 2019 over oceans at nighttime. From up to down represents seasons from spring to winter.

As mentioned in section 3.5, the assumption of dust PSD impacts the $DAOD_{TIR}$ retrieval. In Figure 10, the difference between AERONET and Fennec $DAOD_{10.6\mu m}$ represents the retrieved $DAOD_{TIR}$ uncertainty due to dust PSD assumptions in the TIR observation. However, without the TIR observation, to obtain $DAOD_{TIR}$, we must extend the CALIOP $DAOD_{532nm}$ to the TIR region. How would the extended results be compared to the retrieved $DAOD_{10.6\mu m}$? With this question, we performed the following investigations.

First, we convert the 7-year averaged CALIOP $DAOD_{532nm}$ in summer to be DAOD at 10.6 μm (referred to as "CALIOP $DAOD_{10.6\mu m}$") based on the equation $DAOD_{10.6\mu m} = DAOD_{532nm} \cdot Q_{ext,10.6\mu m}/Q_{ext,532nm}$, where the $Q_{ext,10.6\mu m}/Q_{ext,532nm}$ is introduced in section 3.3 as TIR/VIS ratio. As shown in Figure 5b, Fennec PSDs' TIR/VIS ratio is from 0.35 to 0.5 at 10.6 μm, which can be 4 to 6 times larger than that of AERONET PSD (from 0.05 to 0.14). Consequently, the CALIOP $DAOD_{10.6\mu m}$ based on AERONET PSD is substantially smaller than that based on Fennec PSD (see Figures 11a and 11c), leading to a significant difference (~0.125) between the two CALIOP $DAOD_{10.6\mu m}$ as shown in Figure 11e. Next, we retrieve the corresponding 7-year averaged AERONET $DAOD_{10.6\mu m}$ and Fennec $DAOD_{10.6\mu m}$ as shown in Figures 11b and 11d.

In Figures 11e and 11f, the difference of retrieved $DAOD_{10.6\mu m}$ due to the change of dust PSD is remarkably reduced by ~70% compared with converted CALIOP $DAOD_{10.6\mu m}$. The possible reason is discussed as follows. Firstly, the converted DAOD10.6μm linearly depends on the TIR/VIS ratio, which is highly varied with dust PSD as shown in Figure 5 and previous studies (Figure 7 in Song et al. 2018). Secondly, as the observed dBT provides information on dust extinction, including absorption and scattering, changing the dust PSD assumption varies the dust SSA and g-factor in the retrieval. With the unchanged dust RI, the dependency of g-factor on dust

PSD eventually determines dBT and further the retrieved DAOD10.6μm, as discussed in section 3.5 (see Figures 8a and 8d). Therefore, with the TIR observation, the change of TIR/VIS ratio by dust PSD no longer has an impact on DAOD10.6μm. Instead, the change of dust scattering properties, in this case, the g-factor, by dust PSD determines the difference in the retrieved DAOD10.6μm (see Figures 11f). The moderate variation of dBT based on the change of dust PSD in the retrieval could be the reason leading to a less varied retrieved DAOD10.6μm than the converted DAOD10.6μm. However, we should keep in mind that this result is neither guaranteed in using other TIR wavelengths nor in other combinations of a priori dust assumptions. A more dedicated study is needed for future research.

Moreover, by comparing the CALIOP $DAOD_{10.6\mu m}$ with the retrieved $DAOD_{10.6\mu m}$ based on the same dust PSD in Figure 11, we found that the converted $DAOD_{10.6\mu m}$ using Fennec PSD is more consistent with the TIR observation than using AERONET PSD. This accordance means using the Fennec PSD is more suitable for representing the dust extinction spectrum in both VIS and TIR as Song et al. (2018) suggested at the point of view in dust DRE. It opens an exciting perspective for utilizing the synergic VIS and TIR observation to constraint the $DAOD_{TIR}$, the dust PSD and further the global dust cycle and DRE_{LW} simulation (Song et al. 2018; Wu et al. 2020).

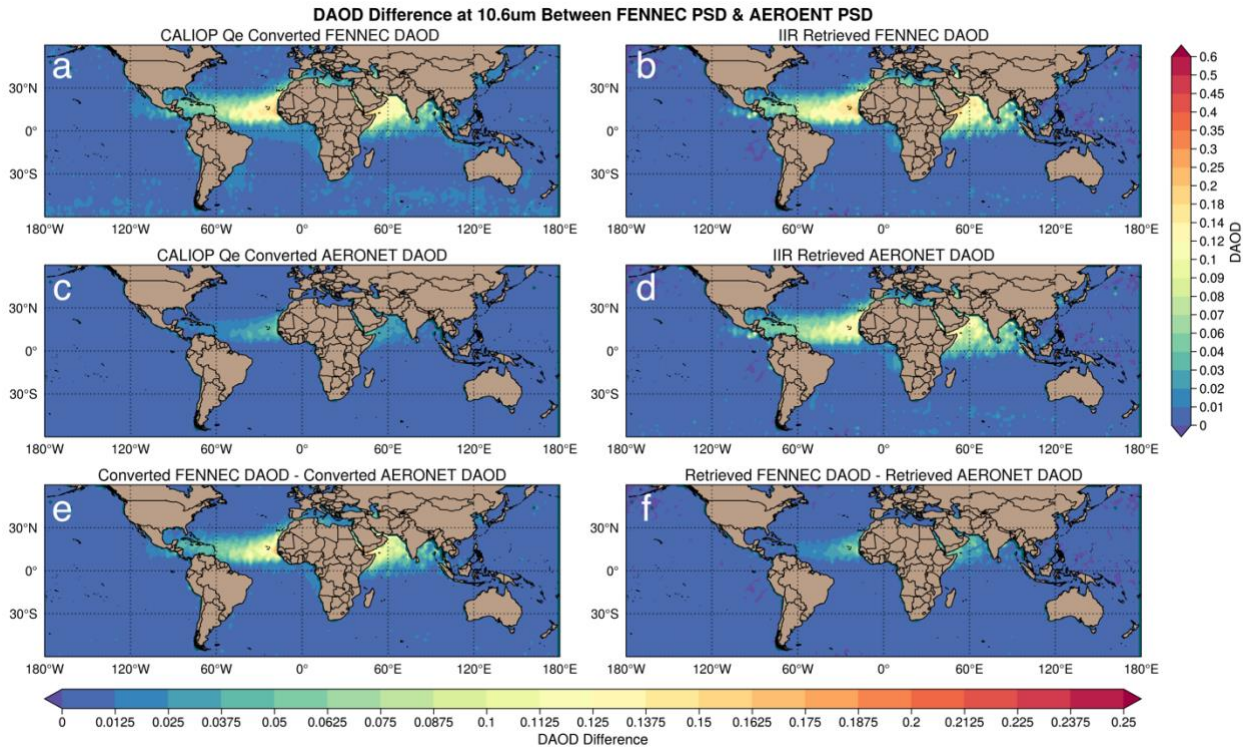

690 Figure 11 The global distribution of a) the mean converted CALIOP $DAOD_{10.6\ \mu m}$ based on Fennec PSD and c) AERONET PSD, and b) the mean retrieved $DAOD_{10.6\ \mu m}$ based on Fennec PSD and d) AERONET PSD, in summer (JJA) of 7-years IIR-CALIOP observation from 2013 to 2019. e) The difference of the mean converted CALIOP $DAOD_{10.6\ \mu m}$ between two PSD assumptions. f) The difference of the mean retrieved $DAOD_{10.6\ \mu m}$ between two PSD assumptions.

Although dust RI has a limited impact on the $DAOD_{TIR}$ retrieval in this study, it is also helpful 695 to see if the TIR observation could constrain the uncertainty due to the dust RI assumptions. In this time, we calculate two CALIOP $DAOD_{10.6\mu m}$ based on the maximum and minimum TIR/VIS ratios corresponding to the variation of regional RIs and the unchanged Fennec PSD (Figures 12a and 12c). Then, the maximum and minimum ones among the retrieved Fennec $DAOD_{10.6\mu m}$ based on the regional RIs are shown in Figures 12b and 12d, respectively. Figure 12e shows that the 700 difference of the two CALIOP $DAOD_{10.6\mu m}$ is substantial over the North Atlantic Ocean, with a mean value of around 0.019. With TIR observation, in Figure 12f, the difference of retrieved

$DAOD_{10.6\mu m}$ under different RI assumptions is reduced by about 26%, except the Sahara Desert's coastal region. The main reason causing this larger change is the alter of dust radiative signal due to the temperature inversion discussed in section 3.5 (see Figures 8d,8e,8f). It is restricted as the impact of temperature inversion is limited in the coastal region near the Saharan Desert. In addition, the absolute DAOD differences caused by RI are only ~37% of that caused by dust PSD. Consequently, the TIR observation also constrains the $DAOD_{TIR}$ uncertainty due to dust RI assumptions if conditions apply, that the TIR channel is less sensitive to dust RI and the atmosphere does not contain strong TI.

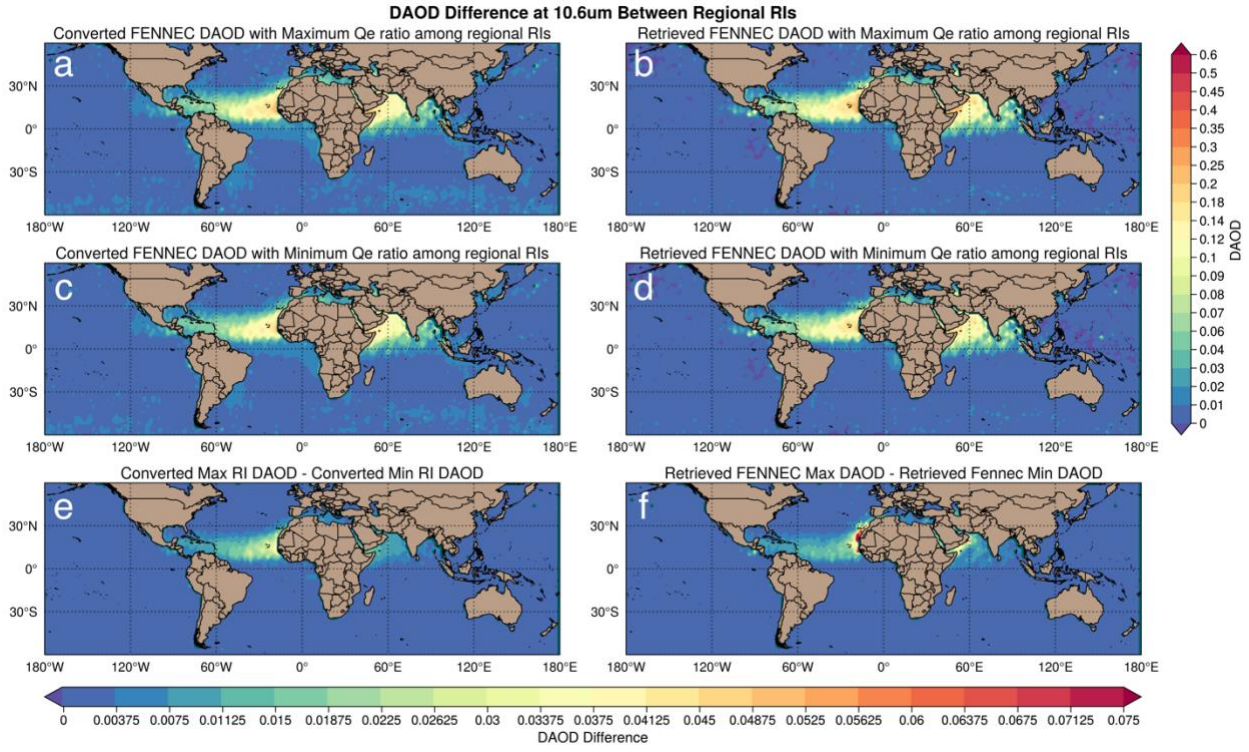

Figure 12 Same as Figure 11, except that the dust PSD is fixed (Fennec PSD) and the difference of assumptions are the regional dust RI with the maximum Q_{ext} ratio and the minimum Q_{ext} ratio.

4.2 Climatology Comparison with IASI-retrieved DAOD

As suggested in the previous section, the Fennec $DAOD_{10.6\mu m}$ makes a better agreement with the theoretically converted CALIOP $DAOD_{10.6\mu m}$. Therefore, to evaluate the IIR-CALIOP retrieval, we compare the Fennec $DAOD_{10.6\mu m}$ with two independent IASI-based DAOD at 10 μm ($DAOD_{10\mu m}$) products developed by different teams. The first one is derived by the group at Laboratoire de Météorologie Dynamique (LMD) (referred to as "IASI-LMD") and the other by the group at Université libre de Bruxelles (ULB) (referred to as "IASI-ULB"). The IASI-LMD algorithm has a long history. It was initiated by Pierangelo et al. (2004) for AIRS and further developed as a decadal dataset for IASI by several follow-up studies (Capelle et al. 2018; Capelle et al. 2014; Peyridieu et al. 2013). It uses a LUT-based retrieval method to retrieve both DAOD at 10 μm and the mean dust layer altitude based on the selected channels of IASI. Instead of using LUTs, the IASI-ULB algorithm utilizes a neural network method to learn the dust spectral characteristics represented by the dust index R based on the observed outgoing longwave spectral radiance (Clarisse et al. 2019). The retrieved DAOD is then obtained by multiplying the observed R with the NN-predicted conversion ratio CR. The NN training process is based on the given atmospheric conditions, dust properties, the monthly mean CALIOP dust altitude and the given IASI observation. As the observed R contains the independent random instrumental noise with a mean of 0, it allows the retrieved DAOD to be negative for reducing bias.

The different spatiotemporal resolution between IASI and CALIPSO prevents enough reliable collocations for the pixel-by-pixel comparison. Here, we only compare the grid-level (i.e., latitude-longitude grid) climatology between Fennec $DAOD_{10.6\mu m}$ and $DAOD_{10\mu m}$ from the IASI products. Note that the IIR-CALIOP retrieval is implemented over oceans at nighttime only, while the current IASI grid-level products include data in the daytime and over lands. To alleviate the sampling difference, we first apply the following filtering procedures for the IASI level-2 (i.e.,

pixel-level) products in 7 years from 2013 to 2019 and then aggregate them to the corresponding grid-level climatological results (2° × 2° grids):

1) Only the nighttime samples over oceans are selected from both IASI products using their surface masks and day/night flags.
2) Only the filtered results after applying the required QA flags in three products are considered. For IIR/CALIOP retrieval, pre_QA <= 1and post_QA = 0 are applied. Quality control processes of IASI retrievals are detailed in Capelle et al. (2018) and Clarisse et al. (2019).

It is necessary to point out that both IASI products do $DAOD_{TIR}$ retrievals on the detected cloud-free pixels with ad hoc dust detection based on the dust TIR spectral patterns. Their cloud masking and dust detection are different from those of the Lidar-based method in the IIR-CALIOP retrieval, leading to the difference in the cloud-free dust sampling. Thus, it should be carried when comparing the 7-year averaged seasonal retrieved DAOD among three products, as shown in Figure 13. Note that there also is a spectral difference of DAOD at 10.0 μm and 10.6 μm, which depends on the assumptions of dust PSD, RI and shape. Therefore, a perfect match of the retrieved DAOD is *not* expected in the comparison. Rather than that, all three products have a good agreement on the seasonal variations of dust transport over NP (in spring), NA and IO (in summer) and TA (in winter), with containable discrepancies of the mean DAOD value, which is listed in Table 4.

In Figure 13, the most apparent discrepancy among $DAOD_{10.6\mu m}$ (left column), IASI-ULB and IASI-LMD $DAOD_{10\mu m}$ (middle and right columns) are over the "background" region with low DAOD (Fennec $DAOD_{10.6\mu m} < 0.01$) as the non-dust aerosol dominates. The IASI-LMD

760 $DAOD_{10\mu m}$ over the "background" region has a significantly larger value (~0.06) than $DAOD_{10.6\mu m}$ ($\leq$ 0.01), especially over the West Pacific "warm pool" and ITCZ, which has high occurrence frequency of cirrus cloud (Prabhakara et al. 1993; Sassen et al. 2008). It implies that the IASI-LMD retrieval technique might overestimate the $DAOD_{10\mu m}$ due to false detected dust radiative signal induced by the sub-pixel cirrus cloud over the "background" region.

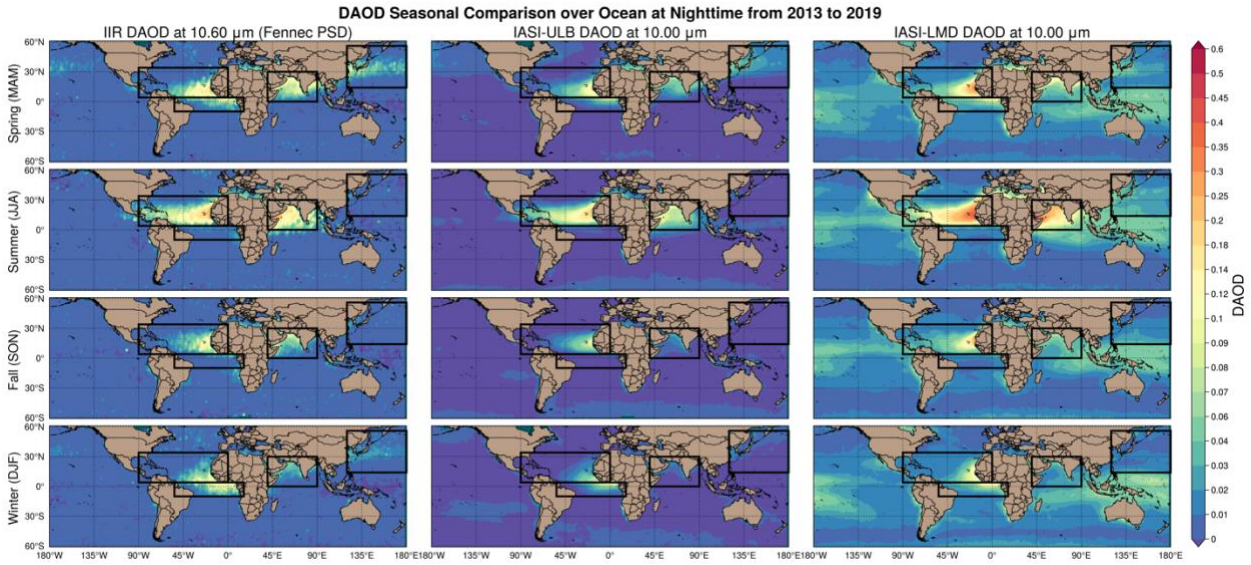

765

Figure 13 The seasonal averaged global distribution of Fennec $DAOD_{10.6\ \mu m}$ (left columns), IASI-ULB $DAOD_{10\mu m}$ (middle columns) and IASI-LMD $DAOD_{10\mu m}$ (right columns). From up to down represents seasons from spring to winter.

To better compare the retrieved DAOD grid-by-grid over the four active dust transport regions, all the grid-level seasonal mean DAODs from three retrieval products over each region are plotted

770 in Figure 14 with linear regression values (i.e., slope, intercept, correlation coefficient (r-value and p-value). The comparison between $DAOD_{10.6\mu m}$ and $DAOD_{10\mu m}$ Over NA (Figure 14a, 14e) and TA (Figure 14b, 14f) shows well-agreed variation as the r-values are higher than 0.8. However, the corresponding slopes deviate from unity, indicating a systematic difference of the absolute value of DAOD, which is also reflected in the mean value comparison in Table 4. Over IO, in

Figures 14c and 14g, $DAOD_{10.6\mu m}$ is still well-agreed with IASI-ULB $DAOD_{10\mu m}$ (r = 0.832), while it has a lower r-value (0.774) with IASI-LMD $DAOD_{10\mu m}$. In Figures 14d and 14h, dust over NP has an overall smaller DAOD (< 0.15) and would also have smaller dust particle size due to the deposition of the coarser particles during the long-term transport from Asia. As a result, the dust radiative signal is harder to be seen in TIR by IASI, leading to higher retrieval uncertainties and, therefore, the lowest r-values (r=0.648 and 0.226) of $DAOD_{10.6\mu m}$ with IASI-ULB and IASI-LMD $DAOD_{10\mu m}$. However, the CALIOP DPR-based dust detection approach can better estimate them based on their non-sphericity but not on their size. Therefore, shown in Figure 13 for over NP in spring and winter, there is a more evident $DAOD_{10.6\mu m}$ trend of dust transport westward than both IASI $DAOD_{10\mu m}$ at around 30°N. It implies that the collocated IIR-CALIOP has a better dust detection performance than that of IASI-only for dust transported from Asia.

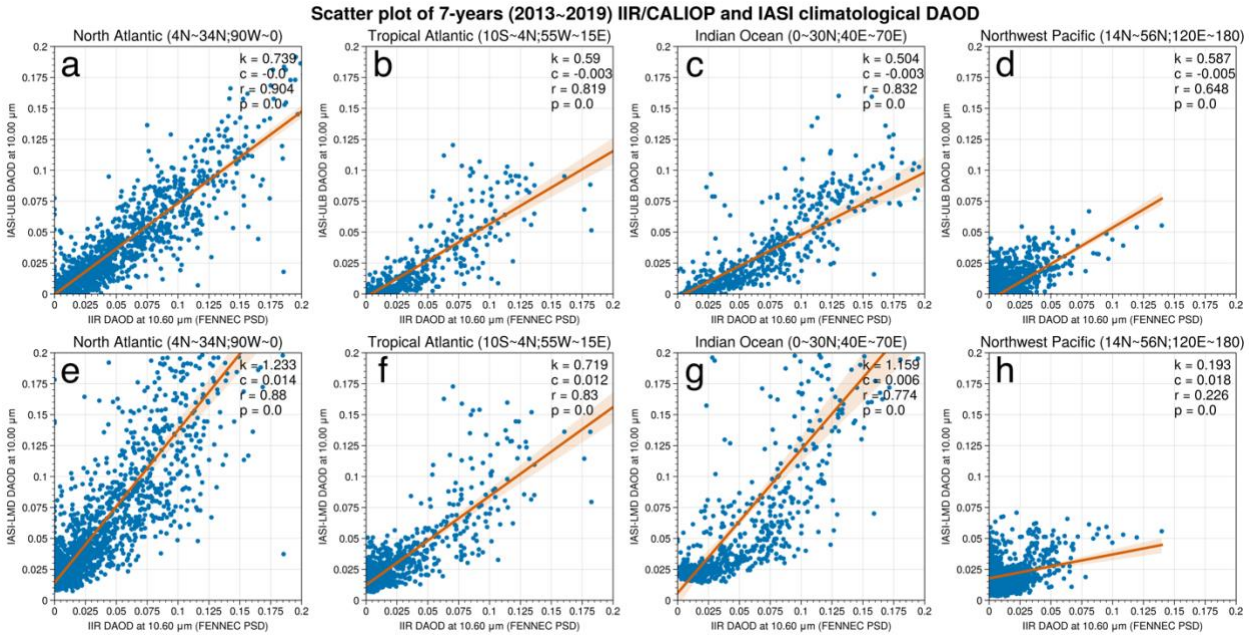

Figure 14 The scatter plot of Fennec $DAOD_{10.6\,\mu m}$ versus IASI-ULB and IASI-LMD $DAOD_{10\mu m}$ over NA (a,e), TA (b,f), IO (c,g) and NP (d,h). Red lines with orange shadow represent the linear regression and its standard error. The k, c, r and p at the upper right of each panel represent the slope, intercept, correlation coefficient and p-value of the linear regression.

In summary, despite the discrepancies over the low DAOD areas, the IIR-CALIOP retrieval is well-agreed with two IASI retrievals on the seasonal variation of dust transport over NA, TA, and IO with confident correlations. In NP, the IIR-CALIOP retrieval reveals a more apparent trend of dust transport than both IASI retrievals at around 30°N. Regarding DAOD value, which is deviated among the three retrievals, further comparison of $DAOD_{10.6\mu m}$ with the well-trusted ground-based AERONET measurement is necessary.

4.3 Seasonal and Interannual Comparison with AERONET Coarse-mode AOD

Most $DAOD_{TIR}$ retrieval studies estimate the results through the collocated comparison with the AERONET coarse-mode AOD in VIS (500 nm; refer to as "AOD_{500nm}") at the dust-dominated sites (Capelle et al. 2018; Capelle et al. 2014; Clarisse et al. 2019; Klüser et al. 2011 (Peyridieu et al. 2013)). However, the simultaneously collocated comparison of CALIPSO with AERONET needs to be within 40 km with a time window of $\pm$30 mins of the overpass time to have a rigorous comparison (Omar et al. 2013; Schuster et al. 2012). In addition, the quantitative comparison with AOD_{500nm} requires the TIR/VIS ratio. With the limited information of dust properties, the assumed TIR/VIS ratio could significantly error the comparison results (Capelle et al. 2018), even if the AOD_{500nm} from dust-dominated sites. Alternatively, in this section, we make the seasonal and interannual comparison of the collocated $1° \times 1°$ monthly mean grid-level $DAOD_{10.6\mu m}$ with AOD_{500nm}. This approach aims to evaluate the consistency between $DAOD_{10.6\mu m}$ and AOD_{500nm}, which has been used to evaluate CALIOP $DAOD_{532nm}$ and AOD_{500nm} (Yu et al. 2015). Without considering the TIR/VIS ratio, it is unnecessary to guarantee the AOD_{500nm} contributed purely by dust. Therefore, we select 97 AERONET sites within the defined dust-concentrated area (see

Figure 1a) over oceans from 2013 to 2019, as shown in Figure 15a. Meanwhile, as a reference, the two monthly mean IASI-retrieved $DAOD_{10\mu m}$ are derived from the IASI-ULB and IASI-LMD level-2 products.

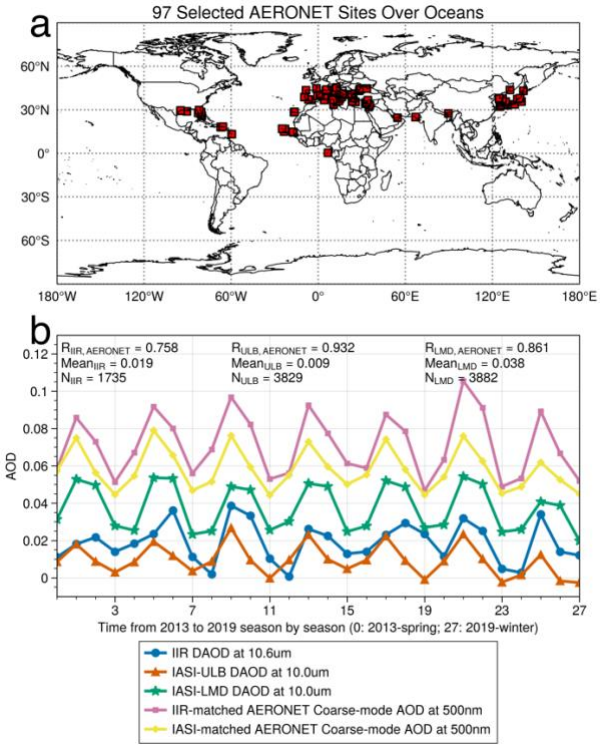

Figure 15 a) The geolocation of 97 selected AERONET sites. b) The seasonal interannual variation of AOD from IIR-CALIOP $DAOD_{10.6\mu m}$ (blue dot), IASI-ULB $DAOD_{10\mu m}$ (red triangle), IASI-LMD $DAOD_{10\mu m}$ (green star) and AERONET AOD_{500nm} paired with IIR-CALIOP (pink square) and IASI (yellow diamond).

In Figure 15b, the correlation coefficient between $DAOD_{10.6\mu m}$ and AOD_{500nm} is 0.754, suggesting that the IIR-CALIOP retrieval agrees reasonably well with AERONET coarse-mode AOD on the seasonal and interannual variations. Because of the higher sampling rate of IASI retrieval than IIR-CALIOP, the IASI-AERONET comparison pairs are 50% more than IIR-AERONET. As a result, we found better correlations in IASI-AERONET comparisons. In addition, the IIR-matched AOD_{500nm} is 17% higher and more fluctuated than IASI-matched AOD_{500nm}. Bearing the +17% difference in the number of pairs, we still found that the interannual mean

$DAOD_{10.6\mu m}$ is 50% larger than IASI-ULB $DAOD_{10\mu m}$ and 50% less than that of $DAOD_{10.6\mu m}$. It implies that the IIR-CALIOP retrieved $DAOD_{10.6\mu m}$ is agrees better with IASI-ULB $DAOD_{10\mu m}$.

5. Summary and Conclusions

This paper introduces a novel way to retrieve $DAOD_{TIR}$ using the integrated CALIOP and IIR observations with a priori dust assumptions based on the state-of-art databases. The retrieval method is based on the BT contrast between the observed BT at the IIR 10.6 μm channel of the cloud-free dust scenario and the simulated cloud-free clean BT with corresponding assumed atmospheric and surface conditions. Thanks to the derived dust vertical distribution from CALIOP, the straightforward LUT depends on DAOD only, which can be built simultaneously with the cloud-free dust detection process. In addition, the 1-km resolution of IIR observation maximally reduces the sub-pixel cloud contamination on the dust radiative signal. Thus, we evaluated the retrieval uncertainties from the instrumental noise, ancillary data, radiative simulation and the a priori dust assumptions and produced climatological retrieval results (i.e., $DAOD_{10.6\mu m}$).

According to the non-spherical dust scattering properties calculation based on the spheroid shape distribution and the Di-Biagio RI databse, the dust PSD assumption is the main contribution to the variation of TIR/VIS ratio in TIR atmospheric window bands, which would produce significantly different $DAOD_{TIR}$ even with identical $DAOD_{VIS}$. However, with the TIR observation, the difference of retrieved $DAOD_{TIR}$ caused by dust PSD assumptions is remarkably reduced. Combing with the synergic VIS observation offers an exciting prospect on constraining the $DAOD_{TIR}$, the dust particle size and further the DRE_{LW} uncertainty.

The comparison between $DAOD_{10.6\mu m}$ and IASI-retrieved $DAOD_{10\mu m}$ developed by the LMD and ULB groups is performed on a 7-year climatological scale with the assurance of sampling procedures. In general, $DAOD_{10.6\mu m}$ shows good agreements of seasonal variations of dust transport with both IASI $DAOD_{10\mu m}$ over the active dust transport regions but with deviations on the mean DAOD. Discrepancies over the low DAOD areas are possibly due to the difference in sampling approach (i.e., cloud masking and dust detection), retrieval methods and the 10.0μm-to-10.6μm spectral difference. Despite that, the consistency of the retrieved $DAOD_{10.6\mu m}$ with AERONET observation is presented through the seasonal and interannual comparison with AERONET coarse-mode AOD over 97 selected sites over oceans.

The study presented here has several limitations. First of all, the limited spatial coverage of CALIOP and the nighttime-only retrieval leads to a relatively low $DAOD_{TIR}$ sampling rate. Secondly, as the highly varied surface emissivity and skin temperature over land would have significant uncertainties, the retrieval is operated over oceans only. Thirdly, the single-band retrieval approach subjects to massive uncertainties from the atmospheric gas absorptions, the instrumental noise, and the radiative transfer simulation. Moreover, it has insufficient information content for retrieving other dust properties such as dust PSD and RI. The retrieval can be improved by adding more information from other channels/instruments and better a priori assumptions. Therefore, the future developments on the current retrieval method to address the remaining challenges are listed below:

1) Propagate the retrieval to the 60-km IIR swath by assuming the vertical distribution of dust from CALIOP within a reasonable scale.

2) Seeking more helpful information from other IIR channels and/or collocated instruments in the A-Train (e.g., MODIS and AIRS) for constraining the retrieval uncertainties, exploring more retrievable properties, and expanding the spatial coverage of the retrieval.

Reference

Adebiyi, A.A., & Kok, J.F. (2020). Climate models miss most of the coarse dust in the atmosphere. Science Advances, 6, eaaz9507

Capelle, V., Chédin, A., Pondrom, M., Crevoisier, C., Armante, R., Crepeau, L., & Scott, N.A. (2018). Infrared dust aerosol optical depth retrieved daily from IASI and comparison with AERONET over the period 2007–2016. *Remote Sensing of Environment, 206*, 15-32

Capelle, V., Chédin, A., Siméon, M., Tsamalis, C., Pierangelo, C., Pondrom, M., Crevoisier, C., Crepeau, L., & Scott, N.A. (2014). Evaluation of IASI-derived dust aerosol characteristics over the tropical belt. *Atmospheric Chemistry & Physics, 14*

Chiapello, I., & Moulin, C. (2002). TOMS and METEOSAT satellite records of the variability of Saharan dust transport over the Atlantic during the last two decades (1979–1997). *Geophysical Research Letters, 29*, 17-11-17-14

Choobari, O.A., Zawar-Reza, P., & Sturman, A. (2014). The global distribution of mineral dust and its impacts on the climate system: A review. *Atmospheric Research, 138*, 152-165

Clarisse, L., Clerbaux, C., Franco, B., Hadji-Lazaro, J., Whitburn, S., Kopp, A.K., Hurtmans, D., & Coheur, P.-F. (2019). A Decadal Data Set of Global Atmospheric Dust Retrieved From IASI Satellite Measurements. *Journal of Geophysical Research: Atmospheres, 124*, 1618-1647

Cuesta, J., Eremenko, M., Flamant, C., Dufour, G., Laurent, B., Bergametti, G., Höpfner, M., Orphal, J., & Zhou, D. (2015). Three-dimensional distribution of a major desert dust outbreak over East Asia in March 2008 derived from IASI satellite observations. Journal of Geophysical Research: Atmospheres, 120, 7099-7127

Di Biagio, C., Banks, J.R., & Gaetani, M. (2021). Dust Atmospheric Transport Over Long Distances. Reference Module in Earth Systems and Environmental Sciences: Elsevier

Di Biagio, C., Formenti, P., Balkanski, Y., Caponi, L., Cazaunau, M., Pangui, E., Journet, E., Nowak, S., Caquineau, S., Andreae, M.O., Kandler, K., Saeed, T., Piketh, S., Seibert, D., Williams, E., & Doussin, J.-F. (2017). Global scale variability of the mineral dust longwave refractive index: a new dataset of in situ measurements for climate modeling and remote sensing. *Atmospheric Chemistry and Physics, 17*, 1901-1929

Di Biagio, C., Balkanski, Y., Albani, S., Boucher, O., & Formenti, P. (2020). Direct Radiative Effect by Mineral Dust Aerosols Constrained by New Microphysical and Spectral Optical Data. Geophysical Research Letters, 47, e2019GL086186

Dubovik, O., Smirnov, A., Holben, B., King, M., Kaufman, Y., Eck, T., & Slutsker, I. (2000). Accuracy assessments of aerosol optical properties retrieved from Aerosol Robotic Network (AERONET) Sun and sky radiance measurements. Journal of Geophysical Research: Atmospheres, 105, 9791-9806

Dubovik, O., Sinyuk, A., Lapyonok, T., Holben, B.N., Mishchenko, M., Yang, P., Eck, T.F., Volten, H., Munoz, O., & Veihelmann, B. (2006). Application of spheroid models to account for aerosol particle nonsphericity in remote sensing of desert dust. *Journal of Geophysical Research: Atmospheres, 111*

Dubovik, O., Holben, B., Eck, T.F., Smirnov, A., Kaufman, Y.J., King, M.D., Tanré, D., & Slutsker, I. (2002). Variability of Absorption and Optical Properties of Key Aerosol Types Observed in Worldwide Locations. Journal of the Atmospheric Sciences, 59, 590-608

Dubuisson, P., Giraud, V., Chomette, O., Chepfer, H., & Pelon, J. (2005). Fast radiative transfer modeling for infrared imaging radiometry. *Journal of Quantitative Spectroscopy and Radiative Transfer, 95*, 201-220

Dubuisson, P., Giraud, V., Pelon, J., Cadet, B., & Yang, P. (2008). Sensitivity of Thermal Infrared Radiation at the Top of the Atmosphere and the Surface to Ice Cloud Microphysics. *Journal of Applied Meteorology and Climatology, 47*, 2545-2560

Dunion, J.P., & Velden, C.S. (2004). The Impact of the Saharan Air Layer on Atlantic Tropical Cyclone Activity. *Bulletin of the American Meteorological Society, 85*, 353-366

Evan, A.T., Dunion, J., Foley, J.A., Heidinger, A.K., & Velden, C.S. (2006). New evidence for a relationship between Atlantic tropical cyclone activity and African dust outbreaks. *Geophysical Research Letters, 33*

Gama, C., Tchepel, O., Baldasano, J.M., Basart, S., Ferreira, J., Pio, C., Cardoso, J., & Borrego, C. (2015). Seasonal patterns of Saharan dust over Cape Verde – a combined approach using observations and modelling. Tellus B: Chemical and Physical Meteorology, 67, 24410

Garnier, A., Pelon, J., Dubuisson, P., Faivre, M., Chomette, O., Pascal, N., & Kratz, D.P. (2012). Retrieval of Cloud Properties Using CALIPSO Imaging Infrared Radiometer. Part I: Effective Emissivity and Optical Depth. *Journal of Applied Meteorology and Climatology, 51*, 1407-1425

Garnier, A., Pelon, J., Pascal, N., Vaughan, M.A., Dubuisson, P., Yang, P., & Mitchell, D.L. (2021). Version 4 CALIPSO Imaging Infrared Radiometer ice and liquid water cloud microphysical properties – Part I: The retrieval algorithms. Atmos. Meas. Tech., 14, 3253-3276

Garnier, A., Scott, N.A., Pelon, J., Armante, R., Crépeau, L., Six, B., & Pascal, N. (2017). Long-term assessment of the CALIPSO Imaging Infrared Radiometer (IIR) calibration and stability through simulated and observed comparisons with MODIS/Aqua and SEVIRI/Meteosat. Atmos. Meas. Tech., 10, 1403-1424

Garnier, A., Trémas, T., Pelon, J., Lee, K.-P., Nobileau, D., Gross-Colzy, L., Pascal, N., Ferrage, P., & Scott, N.A. (2018). CALIPSO IIR Version 2 Level 1b calibrated radiances: analysis and reduction of residual biases in the Northern Hemisphere. *Atmospheric Measurement Techniques, 11*, 2485-2500

Gelaro, R., McCarty, W., Suárez, M.J., Todling, R., Molod, A., Takacs, L., Randles, C.A., Darmenov, A., Bosilovich, M.G., Reichle, R., Wargan, K., Coy, L., Cullather, R., Draper, C., Akella, S., Buchard, V., Conaty, A., da Silva, A.M., Gu, W., Kim, G.-K., Koster, R., Lucchesi, R., Merkova, D., Nielsen, J.E., Partyka, G., Pawson, S., Putman, W., Rienecker, M., Schubert, S.D., Sienkiewicz, M., & Zhao, B. (2017). The Modern-Era Retrospective Analysis for Research and Applications, Version 2 (MERRA-2). *Journal of Climate, 30*, 5419-5454

Goudie, A.S., & Middleton, N.J. (2006). Desert dust in the global system. Springer Science & Business Media

Griffin, D.W. (2007). Atmospheric Movement of Microorganisms in Clouds of Desert Dust and Implications for Human Health. *Clinical Microbiology Reviews, 20*, 459-477

Gutleben, M., Groß, S., Wirth, M., Emde, C., & Mayer, B. (2019). Impacts of water vapor on Saharan air layer radiative heating. *Geophysical Research Letters, 46*, 14854-14862

Hess, M., Koepke, P., & Schult, I. (1998). Optical Properties of Aerosols and Clouds: The Software Package OPAC. *Bulletin of the American Meteorological Society, 79*, 831-844

Kaplan, C. (2013). An Investigation Of Sub-Pixel Cloud/clear-Sky Contamination Using Hyper-Spectral AVIRIS Data

Kim, M.-H., Omar, A.H., Tackett, J.L., Vaughan, M.A., Winker, D.M., Trepte, C.R., Hu, Y., Liu, Z., Poole, L.R., & Pitts, M.C. (2018). The CALIPSO version 4 automated aerosol classification and lidar ratio selection algorithm. *Atmospheric Measurement Techniques, 11*, 6107

Klüser, L., Banks, J.R., Martynenko, D., Bergemann, C., Brindley, H.E., & Holzer-Popp, T. (2015). Information content of space-borne hyperspectral infrared observations with respect to mineral dust properties. Remote Sensing of Environment, 156, 294-309

Klüser, L., Kleiber, P., Holzer-Popp, T., & Grassian, V.H. (2012). Desert dust observation from space – Application of measured mineral component infrared extinction spectra. *Atmospheric Environment, 54*, 419-427

Klüser, L., Martynenko, D., & Holzer-Popp, T. (2011). Thermal infrared remote sensing of mineral dust over land and ocean: a spectral SVD based retrieval approach for IASI. *Atmospheric Measurement Techniques, 4*, 757-773

Kok, J.F., Ridley, D.A., Zhou, Q., Miller, R.L., Zhao, C., Heald, C.L., Ward, D.S., Albani, S., & Haustein, K. (2017). Smaller desert dust cooling effect estimated from analysis of dust size and abundance. Nature Geoscience, 10, 274-278

Liu, Z., Kar, J., Zeng, S., Tackett, J., Vaughan, M., Avery, M., Pelon, J., Getzewich, B., Lee, K.-P., & Magill, B. (2019). Discriminating between clouds and aerosols in the CALIOP version 4.1 data products

Liu, Z., Vaughan, M., Winker, D., Kittaka, C., Getzewich, B., Kuehn, R., Omar, A., Powell, K., Trepte, C., & Hostetler, C. (2009). The CALIPSO lidar cloud and aerosol discrimination: Version 2 algorithm and initial assessment of performance. *Journal of Atmospheric and Oceanic Technology, 26*, 1198-1213

Mahowald, N., Albani, S., Kok, J.F., Engelstaeder, S., Scanza, R., Ward, D.S., & Flanner, M.G. (2014). The size distribution of desert dust aerosols and its impact on the Earth system. Aeolian Research, 15, 53-71

Martins, J.V., Tanré, D., Remer, L., Kaufman, Y., Mattoo, S., & Levy, R. (2002). MODIS cloud screening for remote sensing of aerosols over oceans using spatial variability. *Geophysical Research Letters, 29*, MOD4-1-MOD4-4

Mishchenko, M.I. (2000). Calculation of the amplitude matrix for a non-spherical particle in a fixed orientation. *Applied optics, 39*, 1026-1031

Mishchenko, M.I., Travis, L.D., Kahn, R.A., & West, R.A. (1997). Modeling phase functions for dustlike tropospheric aerosols using a shape mixture of randomly oriented polydisperse spheroids. *Journal of Geophysical Research: Atmospheres, 102*, 16831-16847

Omar, A.H., Winker, D.M., Tackett, J.L., Giles, D.M., Kar, J., Liu, Z., Vaughan, M.A., Powell, K.A., & Trepte, C.R. (2013). CALIOP and AERONET aerosol optical depth comparisons: One size fits none. Journal of Geophysical Research: Atmospheres, 118, 4748-4766

Peyridieu, S., Chédin, A., Tanré, D., Capelle, V., Pierangelo, C., Lamquin, N., & Armante, R. (2010). Saharan dust infrared optical depth and altitude retrieved from AIRS: a focus over North Atlantic – comparison to MODIS and CALIPSO. *Atmospheric Chemistry and Physics, 10*, 1953-1967

Peyridieu, S., Chédin, A., Capelle, V., Tsamalis, C., Pierangelo, C., Armante, R., Crevoisier, C., Crépeau, L., Siméon, M., Ducos, F., & Scott, N.A. (2013). Characterisation of dust aerosols in the infrared from IASI and comparison with PARASOL, MODIS, MISR, CALIOP, and AERONET observations. Atmos. Chem. Phys., 13, 6065-6082

Pierangelo, C., Chédin, A., Heilliette, S., Jacquinet-Husson, N., & Armante, R. (2004). Dust altitude and infrared optical depth from AIRS. *Atmospheric Chemistry and Physics, 4*, 1813-1822

Pierangelo, C., Chédin, A., & Legrand, M. (2013). Longwave passive remote sensing. In J. Lenoble, L. Remer, & D. Tanre (Eds.), Aerosol Remote Sensing (pp. 223-281). Berlin, Heidelberg: Springer Berlin Heidelberg

Prabhakara, C., Kratz, D.P., Yoo, J.M., Dalu, G., & Vernekar, A. (1993). Optically thin cirrus clouds: Radiative impact on the warm pool. Journal of Quantitative Spectroscopy and Radiative Transfer, 49, 467-483

Querol, X., Tobías, A., Pérez, N., Karanasiou, A., Amato, F., Stafoggia, M., Pérez García-Pando, C., Ginoux, P., Forastiere, F., Gumy, S., Mudu, P., & Alastuey, A. (2019). Monitoring the impact of desert dust outbreaks for air quality for health studies. *Environment International, 130*, 104867

Ryder, C.L., Highwood, E.J., Lai, T.M., Sodemann, H., & Marsham, J.H. (2013a). Impact of atmospheric transport on the evolution of microphysical and optical properties of Saharan dust. Geophysical Research Letters, 40, 2433-2438

Ryder, C.L., Highwood, E.J., Rosenberg, P.D., Trembath, J., Brooke, J.K., Bart, M., Dean, A., Crosier, J., Dorsey, J., Brindley, H., Banks, J., Marsham, J.H., McQuaid, J.B., Sodemann, H., & Washington, R. (2013b). Optical

properties of Saharan dust aerosol and contribution from the coarse mode as measured during the Fennec 2011 aircraft campaign. Atmospheric Chemistry and Physics, 13, 303-325

Ryder, C.L., Highwood, E.J., Walser, A., Seibert, P., Philipp, A., & Weinzierl, B. (2019). Coarse and giant particles are ubiquitous in Saharan dust export regions and are radiatively significant over the Sahara. Atmos. Chem. Phys., 19, 15353-15376

Sassen, K., Wang, Z., & Liu, D. (2008). Global distribution of cirrus clouds from CloudSat/Cloud-Aerosol Lidar and Infrared Pathfinder Satellite Observations (CALIPSO) measurements. Journal of Geophysical Research: Atmospheres, 113

Satheesh, S.K., & Moorthy, K.K. (2005). Radiative effects of natural aerosols: A review. *Atmospheric Environment, 39*, 2089-2110

Schuster, G.L., Vaughan, M., MacDonnell, D., Su, W., Winker, D., Dubovik, O., Lapyonok, T., & Trepte, C. (2012). Comparison of CALIPSO aerosol optical depth retrievals to AERONET measurements, and a climatology for the lidar ratio of dust. Atmos. Chem. Phys, 12, 7431-7452

Sokolik, I.N., Toon, O.B., & Bergstrom, R.W. (1998). Modeling the radiative characteristics of airborne mineral aerosols at infrared wavelengths. *Journal of Geophysical Research: Atmospheres, 103*, 8813-8826

Song, Q., Zhang, Z., Yu, H., Kato, S., Yang, P., Colarco, P., Remer, L.A., & Ryder, C.L. (2018). Net radiative effects of dust in the tropical North Atlantic based on integrated satellite observations and in situ measurements. *Atmospheric Chemistry and Physics, 18*, 11303-11322

Stamnes, K., Tsay, S.C., Wiscombe, W., & Jayaweera, K. (1988). Numerically stable algorithm for discrete-ordinate-method radiative transfer in multiple scattering and emitting layered media. *Applied optics, 27*, 2502-2509

Tegen, I., & Lacis, A.A. (1996). Modeling of particle size distribution and its influence on the radiative properties of mineral dust aerosol. *Journal of Geophysical Research: Atmospheres, 101*, 19237-19244

Tegen, I., Lacis, A.A., & Fung, I. (1996). The influence on climate forcing of mineral aerosols from disturbed soils. *Nature, 380*, 419-422

Torres, O., Bhartia, P., Herman, J., Ahmad, Z., & Gleason, J. (1998). Derivation of aerosol properties from satellite measurements of backscattered ultraviolet radiation: Theoretical basis. *Journal of Geophysical Research: Atmospheres, 103*, 17099-17110

Vaughan, M.A., Winker, D.M., & Powell, K.A. (2005). CALIOP algorithm theoretical basis document, part 2: Feature detection and layer properties algorithms. Rep. PC-SCI, 202, 87

Volz, F.E. (1973). Infrared optical constants of ammonium sulfate, sahara dust, volcanic pumice, and flyash. Applied optics, 12, 564-568

Winker, D.M., Tackett, J.L., Getzewich, B.J., Liu, Z., Vaughan, M.A., & Rogers, R.R. (2013). The global 3-D distribution of tropospheric aerosols as characterized by CALIOP. Atmos. Chem. Phys., 13, 3345-3361

Wong, S., Dessler, A.E., Mahowald, N.M., Yang, P., & Feng, Q. (2009). Maintenance of Lower Tropospheric Temperature Inversion in the Saharan Air Layer by Dust and Dry Anomaly. *Journal of Climate, 22*, 5149-5162

Wu, M., Liu, X., Yu, H., Wang, H., Shi, Y., Yang, K., Darmenov, A., Wu, C., Wang, Z., Luo, T., Feng, Y., & Ke, Z. (2020). Understanding processes that control dust spatial distributions with global climate models and satellite observations. Atmos. Chem. Phys., 20, 13835-13855

Xia, X.-a., Chen, H.-b., & Wang, P.-c. (2004). Validation of MODIS aerosol retrievals and evaluation of potential cloud contamination in East Asia. *Journal of Environmental Sciences, 16*, 832-837

Yang, W., Marshak, A., Várnai, T., Kalashnikova, O.V., & Kostinski, A.B. (2012). CALIPSO observations of transatlantic dust: vertical stratification and effect of clouds. Atmos. Chem. Phys., 12, 11339-11354

Young, S.A., Vaughan, M.A., Garnier, A., Tackett, J.L., Lambeth, J.D., & Powell, K.A. (2018). Extinction and optical depth retrievals for CALIPSO's Version 4 data release. *Atmospheric Measurement Techniques, 11*

Young, S.A., Vaughan, M.A., Kuehn, R.E., & Winker, D.M. (2013). The retrieval of profiles of particulate extinction from Cloud–Aerosol Lidar and Infrared Pathfinder Satellite Observations (CALIPSO) data: Uncertainty and error sensitivity analyses. *Journal of Atmospheric and Oceanic Technology, 30*, 395-428

Yu, H., Chin, M., Winker, D.M., Omar, A.H., Liu, Z., Kittaka, C., & Diehl, T. (2010). Global view of aerosol vertical distributions from CALIPSO lidar measurements and GOCART simulations: Regional and seasonal variations. Journal of Geophysical Research: Atmospheres, 115

Yu, H., Chin, M., Bian, H., Yuan, T., Prospero, J.M., Omar, A.H., Remer, L.A., Winker, D.M., Yang, Y., & Zhang, Y. (2015). Quantification of trans-Atlantic dust transport from seven-year (2007–2013) record of CALIPSO lidar measurements. *Remote Sensing of Environment, 159*, 232-249

Yu, H., Kaufman, Y., Chin, M., Feingold, G., Remer, L., Anderson, T., Balkanski, Y., Bellouin, N., Boucher, O., & Christopher, S. (2006). A review of measurement-based assessments of the aerosol direct radiative effect and forcing

Zhou, D.K., Larar, A.M., & Liu, X. (2013). MetOp-A/IASI Observed Continental Thermal IR Emissivity Variations. IEEE Journal of Selected Topics in Applied Earth Observations and Remote Sensing, 6, 1156-1162